

Ice-proximal sea-ice reconstruction in Powell Basin, Antarctica since the Last Interglacial

Wee Wei Khoo^{1*}, Juliane Müller^{1,2,3}, Oliver Esper¹, Wenshen Xiao⁴, Christian Stepanek¹, Paul Gierz¹, Gerrit Lohmann^{1,3,5}, Walter Geibert¹, Jens Hefter¹ and Gesine Mollenhauer^{1,2,3}

¹Alfred Wegener Institute, Helmholtz Centre for Polar and Marine Research, Bremerhaven, Germany

²Department of Geoscience, University of Bremen, Bremen, Germany

³MARUM - Center for Marine Environmental Sciences, University of Bremen, Bremen, Germany

⁴State Key Laboratory of Marine Geology, Tongji University, Shanghai, China

⁵Department of Environmental Physics, University of Bremen, Bremen, Germany

Correspondence: Wee Wei Khoo (wee.wei.khoo@awi.de)

ABSTRACT. In Antarctica, the presence of sea ice not only plays a critical role in the climate system but also contributes to enhancing the stability of the floating ice shelves. Hence, investigating past ice-proximal sea-ice conditions, especially across glacial-interglacial cycles, can provide crucial information pertaining to sea-ice variability and deepen our understanding of ocean-ice-atmosphere dynamics and feedback. In this study, we apply a multiproxy approach, in combination with numerical climate modeling, to explore glacial-interglacial environmental variability. We analyze the novel sea ice biomarker IPSO₂₅ (a di-unsaturated highly branched isoprenoid (HBI)), open-water biomarkers (tri-unsaturated HBIs; z-/e-trienes), and the diatom assemblage and primary productivity indicators in a marine sediment core retrieved from Powell Basin, NW Weddell Sea. These biomarkers have been established as reliable proxies for reconstructing near-coastal sea-ice conditions in the Southern Ocean, where the typical use of sea ice-related diatoms can be impacted by silica dissolution. We present the first continuous sea-ice records, in close proximity to the Antarctic continental margin, since the penultimate deglaciation. Our data shed new light on the (seasonal) variability of sea ice in the basin, and reveal a highly dynamic glacial-interglacial sea-ice setting characterized by significant shifts from perennial ice cover to seasonal sea-ice cover and open marine environment over the last 145 kyrs. Our results also unveil a stronger deglacial amplitude and warming during the Last Interglacial (MIS 5e) compared to the current one (Holocene). A short-term sea ice readvancement also occurred towards the end of each deglaciation. Finally, despite similar findings between the proxy and model data, notable differences persist between both interglacials – emphasizing the necessity for different Antarctic ice-sheet configurations to be employed and more robust paleoclimate data to enhance climate model performance close to the Antarctic continental margin.

33 1 Introduction

34 Sea ice plays a vital role within Earth's climate system, exerting significant influence on air-sea
35 interactions, ocean circulation and ecosystem dynamics. Its presence alters the surface albedo of the
36 ocean through the reflectance of incoming solar radiation, thereby minimizing ocean warming (Ebert et
37 al., 1995). Likewise, sea ice affects the atmosphere-ocean interaction by inhibiting the exchange of
38 heat, gas and water vapor between both media (Dieckmann and Hellmer, 2010). During sea-ice
39 formation, brine rejection occurs and leads to the production of high-saline shelf water. This dense high-
40 saline shelf water then sinks towards the deeper ocean. Consequently, this process results in
41 redistribution of salinity within the water column and has a profound impact on the stratification and
42 ventilation of the ocean (Vaughan et al., 2013). For example, in a few locations in the Southern Ocean
43 (SO), such as the Weddell Sea, the high-saline shelf water – depending on its route and mixing process
44 – becomes the precursor of Antarctic Bottom Water (AABW), which is a major driver of the global
45 thermohaline circulation and an important water mass that ventilates the deep ocean basins (Naveira
46 Garabato et al., 2002; Rintoul, 2018; Seabrooke et al., 1971). Furthermore, when sea ice melts, the
47 freshened surface water mixes with the upwelled deep water, contributing to the mode and intermediate
48 waters in the Atlantic, Indian and Pacific sectors of the SO (Abernathy et al., 2016; Pellichero et al.,
49 2018). Sea ice also serves as a crucial buttressing force at the ice front, effectively preventing or
50 delaying the occurrence of potential calving events (Robel, 2017). This phenomenon was evident at
51 locations such as the Mertz Glacier Tongue (Massom et al., 2015) and the Totten Ice Shelf (Greene et
52 al., 2018) in East Antarctica. Furthermore, the presence of a sea-ice buffer in front of the ice terminus
53 acts to diminish ocean swells as they propagate towards land. For instance, Massom et al. (2018)
54 observed a substantial increase (orders of magnitude) in wave energy experienced at the fronts of the
55 Larsen ice shelves and the Wilkins Ice Shelf when the sea-ice buffer was removed. In this regard, any
56 changes to the sea-ice cover can potentially alter ice-ocean-atmosphere dynamics and ocean
57 circulation patterns, making analyses of sea-ice variability over glacial-interglacial cycles, covering
58 periods of less and more pronounced sea-ice cover, crucial.

59 Presently, numerous methods are used to reconstruct past sea-ice conditions, including biogenic
60 proxies (e.g., biomarkers, diatoms, dinoflagellate cysts, foraminifera and ostracods) and
61 sedimentological proxies (e.g., ice-rafted debris) in marine sediments, as well as chemical compounds
62 archived in ice cores (e.g., methanesulfonic acid and sea-salt (ssNa⁺); de Vernal et al., 2013 and
63 references therein). Determination of methanesulfonic acid or ssNa⁺ concentrations in Antarctic ice
64 cores permits well-dated and temporally high-resolution regional sea-ice reconstructions but is often
65 affected by other sea ice independent factors such as atmospheric transport (Abram et al., 2013). In
66 particular, direct proxies, originating from sea-ice dwelling microorganisms, which are preserved in
67 marine sediments are often preferred as they increase the reliability of sea-ice estimation (Leventer,
68 1998). Despite this, our understanding of past sea ice changes in the SO remains limited. The Cycles
69 of Sea-Ice Dynamics in the Earth System working group (C-SIDE; Chadwick et al., 2019; Rhodes et al.,
70 2019) consolidated a list of published Antarctic marine sea-ice records, as outlined in the review paper
71 by Crosta et al. (2022). The compilation documents 20 studies on sea-ice variability during the Holocene
72 (0-12 ka before present (BP)), 150 records detailing changes at the Last Glacial Maximum (LGM; ca.

73 21 ka BP or Marine Isotope Stage (MIS) 2), and a mere 14 sea-ice records dating back to around 130
74 ka BP. Notably, just two records extend beyond MIS 6 (ca. 191 ka BP; see also Fig. 3 in Crosta et al.,
75 2022). Their work underscores the pronounced dearth of (paleo) sea-ice reconstructions, particularly in
76 regions south of 60°S, notably in the Atlantic sector, and during the Last Interglacial (LIG) and beyond.
77 This scarcity of records, in particular proximal to the continental margin, is attributable to difficulties in
78 recovering marine sediment cores in the polar regions that at present are still subject to heavy year-
79 round ice cover, and a lack of continuous sedimentary records due to erosion and disturbance at the
80 sea floor during past glaciations. Moreover, limited preservation potential of silica frustules in SO
81 regions outside of the opal belt further hampers sea-ice reconstructions using diatom assemblages
82 (Ryves et al., 2009; Vernet et al., 2019). As such, important feedback mechanisms related to the sea
83 ice-ice shelf system during warmer-than-present periods and throughout climate transitions, remain
84 poorly understood. Ultimately, this lack of knowledge on how Antarctic ice sheets/shelves respond(ed)
85 to oceanic forcing may disadvantage climate models' ability to faithfully reproduce dynamics in the
86 ocean-sea ice-ice system, and limit our confidence in future projections of the Antarctic Ice Sheet's
87 contribution towards global sea level rise (Deconto and Pollard, 2016; Naughten et al., 2018). Despite
88 similar LIG winter sea-ice (WSI) retreats in marine records, inconsistency with regard to the position of
89 the sea-ice edge, in particular in the Atlantic sector, remains evident when the proposed spatial structure
90 of the $\delta^{18}\text{O}$ -agreed WSI extent is compared to published marine records (Holloway et al., 2017).
91 Holloway et al. (2017) and Crosta et al. (2022) opined that this discrepancy may result from the marine
92 records (Bianchi and Gersonde, 2002; Chadwick et al., 2020; 2022) being located too far north to
93 adequately validate the $\delta^{18}\text{O}$ -agreed WSI extent. Thus, they emphasized the need for additional marine
94 records closer to the continental margin to adequately constrain the spatial pattern of the LIG sea-ice
95 extent.

96 In recent years, the use of a novel sea-ice biomarker has been found increasingly applicable as a
97 suitable proxy for Antarctic sea-ice reconstructions (Belt et al., 2016; Smik et al., 2016). This sea-ice
98 biomarker, a di-unsaturated C_{25} highly branched isoprenoid (HBI) alkene, introduced as an Antarctic
99 sea-ice proxy by Massé et al. (2011), was later termed Ice Proxy for the Southern Ocean with 25 carbon
100 atoms (IPSO₂₅), drawing parallel to the Arctic IP₂₅ (Belt et al., 2016). IPSO₂₅ is a lipid molecule produced
101 by the sympagic diatom *Berkeleya adeliensis*, which lives in the sea-ice matrix and is generally
102 abundant during late spring and early summer (Belt et al., 2016; Riaux-Gobin and Poulin, 2004), hence,
103 making the biomarker a good indicator for spring/summer sea ice. Furthermore, the biomarker is well-
104 preserved in the sediment and widely identified in areas near to the Antarctic continent (for more details,
105 see Belt, 2018; Belt et al., 2016). Nevertheless, there remains a risk of under-/overestimating the
106 presence of sea ice when relying solely on the IPSO₂₅ proxy. Thus, Vorrath et al. (2019) proposed
107 combining open-water phytoplankton markers like dinosterol or a HBI-triene with the IPSO₂₅ proxy, to
108 calculate the phytoplankton-IPSO₂₅ index (PIPSO₂₅). This enhances the quantitative application of the
109 IPSO₂₅ proxy. For example, in cases where the IPSO₂₅ concentration is minimal or absent, this may
110 imply either an open ocean condition (substantiated by a high phytoplankton signal) or the presence of
111 a perennial ice cover (evident by a low/absent phytoplankton signal). As such, the use of the PIPSO₂₅
112 proxy proves to be a more reliable approach to distinguish contrasting sea-ice settings (Belt and Müller,

113 2013; Lamping et al., 2020). To substantiate this application, Lamping et al. (2021) compared PIPSO₂₅-
114 derived sea-ice estimates close to the Antarctic continental margin against satellite sea-ice
115 observations and modeled sea-ice patterns, revealing strong correlation between the proxy, satellite
116 and modeled data. Until now, the majority of HBI-based sea-ice reconstructions has focused on
117 Holocene and deglacial/LGM time scales (e.g., Barbara et al., 2013; 2016; Denis et al., 2010; Etourneau
118 et al., 2013; Lamping et al., 2020; Sadatzki et al., 2023; Vorrath et al., 2020, 2023) and one
119 reconstruction dates back to the last ca. 60 ka BP (Collins et al., 2013). Yet, this tool has not been
120 applied towards studying sea-ice variability in the Antarctic during warm climates beyond the current
121 interglacial.

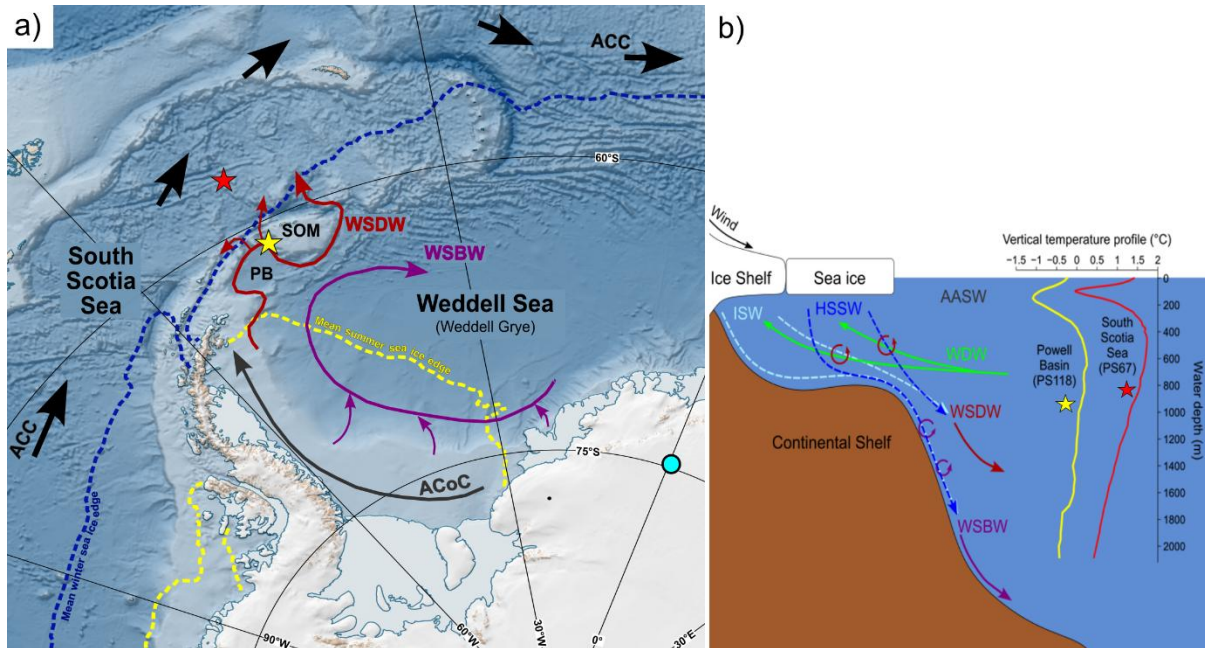
122 Here, we aim to investigate the glacial-interglacial environmental variability in the Powell Basin,
123 NW Weddell Sea through a multiproxy approach, and provide the first continuous ice-proximal Antarctic
124 sea-ice record covering the last ca. 145 kyrs. We present biomarker-based reconstructions of sea ice,
125 subsurface ocean temperature, total organic carbon (TOC) and biogenic silica (bSiO₂) content, as well
126 as diatom-based sea-ice concentration and summer sea surface temperature (SSST). This information
127 is complemented by reconstructions of sea ice, primary productivity and SSST records from a
128 neighboring core in the South Scotia Sea as well as numerically modeled sea ice, sea surface and
129 subsurface temperatures to track latitudinal shifts in the environmental development in the Atlantic
130 sector of the SO.

131 **2 Study area**

132 The Powell Basin (Fig. 1a) is a semi-isolated basin situated in the northwestern part of the Weddell
133 Sea. It has an area of approximately 5×10^4 km² and an average water depth of 3.3 km (Coren et al.,
134 1997; Viseras and Maldonado, 1999). The basin, enclosed by the Antarctic Peninsula to the west, the
135 South Scotia Sea to the north, the South Orkney Microcontinent to the east, and the Weddell Sea to
136 the South, is at present subject to the clockwise-circulating regime of the Weddell Gyre. As described
137 in Orsi et al. (1993) and Vernet et al. (2019), the gyre involves four main water masses, namely Antarctic
138 Surface Water, Warm Deep Water (WDW), Weddell Sea Deep Water (WSDW) and Weddell Sea
139 Bottom Water (WSBW; Fig. 1b). The Antarctic Surface Water generally consists of shelf waters formed
140 over the continental shelf, such as winter water, high salinity shelf water from brine rejection due to sea-
141 ice formation, and ice-shelf water from glacial melt. The shelf waters travel along the Weddell Sea
142 continental shelf via the Antarctic Coastal Current while denser shelf water cascades down and along
143 the continental slope as the Antarctic Slope Current (Deacon, 1937; Fahrbach et al., 1992; Jacobs,
144 1991; Thompson et al., 2018). The WDW originates from the warm, saline and low-oxygen Antarctic
145 Circumpolar Current that is advected and subsequently integrated into the gyre's circulation at its
146 eastern front (Orsi et al., 1993; 1995). Along the southern boundary of the Weddell Gyre, the WDW
147 upwells close to the Antarctic margin and mixes with the Antarctic Surface Water. The admixture cools
148 and becomes denser, giving rise to the formation of WSDW and WSBW water masses at deeper water
149 depths (Carmack and Foster, 1975; Dorschel, 2019; Huhn et al., 2008). In the Powell Basin, part of the
150 WSDW flows out into the Scotia Sea through channels on the western slope of the basin (namely Philip,

151 Bruce and Discovery Passages; Morozov et al., 2020). The remaining WSDW and a part of WSBW
 152 navigate around the southern and eastern South Orkney Plateau, progressing northward via the Orkney
 153 Passage as AABW, while the residual WSBW recirculates within the Weddell Gyre (Fedotova and
 154 Stepanova, 2021; Gordon et al., 2001; Orsi et al., 1999).

155



156
 157 **Figure 1. a)** Map of the study area showing the locations of marine sediment cores PS118_63-1 (yellow
 158 star), PS67/219-1 (red star) and EDML ice core (light blue circle) discussed in this paper. Mean winter and
 159 summer sea-ice extent (1981-2010; Fetterer et al., 2017) are illustrated by blue and yellow dotted lines,
 160 respectively. Map was adapted from the Norwegian Polar Institute's Qantarctica package using QGIS 3.28
 161 (Matsuoka et al., 2018). **b)** Diagram of the Weddell Gyre water masses with vertical spring/summer
 162 temperature profiles collected near to our core sites in Powell Basin (-61.125°S, -47.675°W) and South
 163 Scotia Sea (-57.125°S, -42.375°W; World Ocean Atlas 18; Locarnini et al., 2018). Pathways of ocean currents
 164 (ACC: Antarctic Circumpolar Current – black; ACoC: Antarctic Coastal Current – grey) and water masses
 165 (ISW: Ice Shelf Water – light blue; HSSW: High Saline Shelf Water – blue; WDW: Warm Deep Water – green;
 166 WSDW: Weddell Sea Deep Water – red and WSBW: Weddell Sea Bottom Water – dark magenta) are
 167 represented by the colored arrows. AASW: Antarctic Surface Water, PB: Powell Basin, SOM: South Orkney
 168 Microcontinent.

169 3 Materials and methods

170 3.1 Sediment core and age model

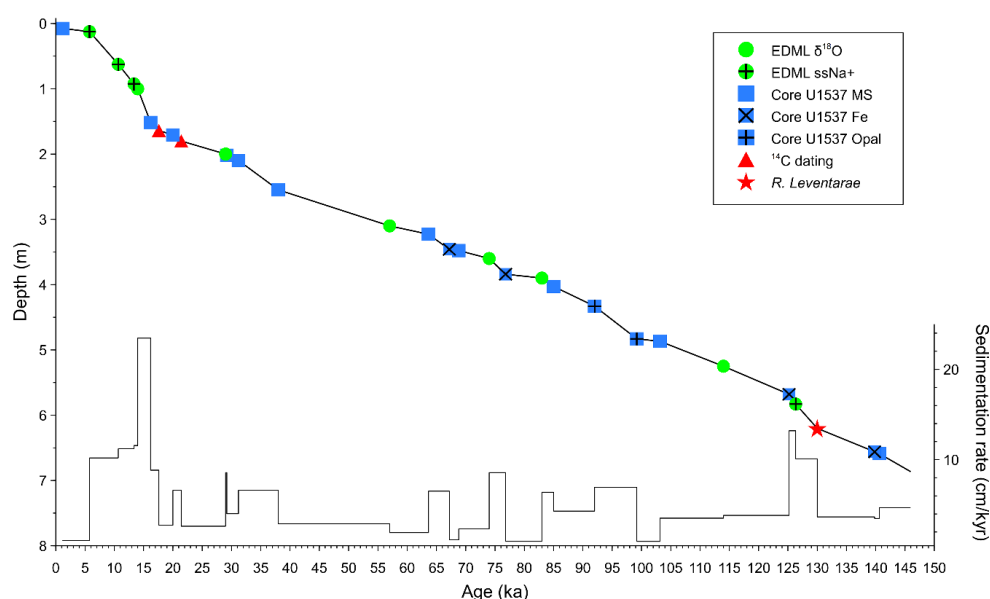
171 Gravity core PS118_63-1 was recovered from the Powell Basin during the RV *Polarstern* cruise
 172 PS118 to the Weddell Sea in 2019 (Fig. 1a; Table 1; Dorschel, 2019). Physical properties, such as
 173 magnetic susceptibility (MS) and wet-bulk density, were provided by Frank Niessen (shipboard data;
 174 Dorschel, 2019). The age model of core PS118_63-1 is based on ¹⁴C radiocarbon dates, the
 175 identification of the biostratigraphic marker *Rouxia leventerae*, as well as tuning against records from
 176 the EDML ice core ($\delta^{18}\text{O}$ and ssNa+) and nearby marine sediment core U1537 (MS, XRF-Fe and opal;
 177 Weber et al., 2022). Refer also to Fig. 2 and Supplementary Table S2 for the tie points. Our age model
 178 is further substantiated by age constraints of the uranium series disequilibrium, in particular the
 179 constant-rate-of-supply model for ²³⁰Th-excess (Geibert et al., 2019). Further details on the
 180 establishment of the age model and methods are provided in Supplement S1 and S2.

181

182 **Table 1. Locations and details of investigated and discussed cores.**

Station	Latitude	Longitude	Water depth / Elevation (m)	Recovery (m)	Data source
Marine sediment cores					
PS118_63-1	61° 07.421'S	47° 44.028'W	2626.5	6.88	this study
PS67/219-1	57° 13.22'S	42° 28.02'W	3619	20.71	this study; Xiao et al, 2016a; Xiao et al, 2016b
Ice core					
EDML	75°S	0°	2891		EPICA Community Members, 2006; Fischer et al, 2007

183



184

185 **Figure 2. Tie points used for the age-depth model of PS118_63-1 and sedimentation rates. EDML ice core**
 186 **data is indicated by green circles, marine core U1537 data is marked by navy blue square, and available**
 187 **AMS ¹⁴C dates and the biostratigraphic marker (*R. leventerae*) from core PS118_63-1 are depicted by red**
 188 **triangles (¹⁴C dates) and a red star (*R. leventerae*).**

189 **3.2 Bulk and organic geochemical analyses**

190 A total of 108 sediment samples, each with an approximate thickness of 1 cm, were collected from
 191 core PS118_63-1. These samples were then freeze-dried and homogenized using an agate mortar and
 192 pestle. All samples were stored in glass vials at -20 °C to prevent degradation. To analyze total organic
 193 carbon (TOC), about 0.1 g of sediment was treated with 500 μL of hydrochloric acid to remove any
 194 inorganic carbon, including carbonates. After the treatment, the TOC content was measured using a
 195 carbon-sulfur analyzer (ELTRA CS800). Routine analyses of standard sediments were conducted
 196 before and during each measurement yielding an error of ±0.02%. Biogenic opal was determined using
 197 the automated continuous wet-chemical leaching method prescribed in Müller and Schneider (1993)
 198 with an error of ±2 wt.%. For biomarker analyses, around 5-8 g of sediment were extracted and purified
 199 in accordance with well-established protocols (Belt et al., 2012; Lamping et al., 2021). Prior to

200 extraction, internal standards, 7-hexylnonadecane (7-HND) and C₄₆-GDGT, were added for subsequent
201 quantification of HBIs and glycerol dialkyl glycerol tetraether (GDGT) lipids. The biomarkers were
202 extracted via ultrasonication (3 x 15 min) using DCM:MeOH (3 x 10 mL; 2:1 v/v) as solvent. Thereafter,
203 the extracts were fractionated via open-column chromatography, with SiO₂ as the stationary phase, with
204 the HBI-containing fractions eluted with 5 mL *n*-hexane and the GDGT fractions with 5 mL DCM:MeOH
205 (1:1 v/v).

206 Compound analyses of HBIs were performed using an Agilent 7890B Gas Chromatograph (GC;
207 fitted with a 30 m DB 1MS column; 0.25 mm diameter and 0.250 μm film thickness) coupled to an
208 Agilent 5977B Mass Selective Detector (MSD; with 70 eV constant ionization potential, ion source
209 temperature of 230°C). The GC oven temperature was first set to 60°C (3 min), then to 150°C (heating
210 rate of 15°C/min), and finally to 320°C (heating rate of 10°C/min), at which it was held for 15 min for the
211 analysis. Helium was used as the carrier gas. Specific compound identification was based on their
212 retention times and mass spectra characteristics (Belt, 2018; Belt et al., 2000).

213 Quantification of each biomarker was based on setting the manually integrated GC-MS peak area
214 relative to corresponding internal standards and instrumental-compound response factors. The
215 concentrations were subsequently corrected to the extracted sediment weight. For HBI quantification,
216 the molecular ions *m/z* 348 (IPSO₂₅) and *m/z* 346 (*z*-/*e*-trienes) were used in relation to its internal
217 standard 7-HND (*m/z* 266). Finally, all biomarker mass concentrations were normalized to the TOC
218 content of each sample. For calculating PIPSO₂₅, we adopted the equation as described in Vorrath et
219 al. (2019):

$$\text{PIPSO}_{25} = \text{IPSO}_{25} / (\text{IPSO}_{25} + (\text{phytoplankton marker} \times c)), \quad (1)$$

220 where *c* is the ratio between the mean concentrations of IPSO₂₅ and phytoplankton marker and
221 balances any significant offsets between both biomarker concentrations (Müller et al., 2011).

222 The GDGT fraction was dried (N₂) and redissolved in 120 μL hexane-isopropanol alcohol (99:1
223 v/v), followed by filtration through a polytetrafluoroethylene (PTFE) filter with 0.45 μm pore size
224 membrane. GDGT measurement was performed using an Agilent 1200 series high-performance liquid
225 chromatograph coupled to an Agilent 6120 atmospheric pressure chemical ionization mass
226 spectrometer. Identification of isoprenoid GDGTs (isoGDGTs) and branched GDGTs (brGDGTs) was
227 based on retention times and mass-to-charge ratios (isoGDGTs: *m/z* 1302, 1300, 1298, 1296 and 1292;
228 brGDGTs: *m/z* 1050, 1036 and 1022). The late eluting hydroxylated-GDGTs (OH-GDGTs) with
229 molecular ions *m/z* 1318, 1316 and 1314 were also determined during the scan of related isoGDGTs,
230 namely *m/z* 1300, 1298 and 1296, respectively (Liu et al., 2012a; 2012b). The relative abundances
231 were subsequently quantified relative to internal standard C₄₆ (*m/z* 744), instrumental response factors
232 and the amount of sediment extracted. Mass content of all GDGTs were normalized to the TOC content
233 of each sample.

234 The isoGDGT-based index, TEX₈₆^L (Eq 2) was calculated following Kim et al. (2010) while the
235 conversion to subsurface ocean temperature (OT; 0 - 200 m water depth; Eq 3) was conducted in
236 accordance to Hagemann et al. (2023):

$$\text{TEX}_{86}^L = \text{Log}_{10} \frac{[\text{isoGDGT-2}]}{[\text{isoGDGT-1}] + [\text{isoGDGT-2}] + [\text{isoGDGT-3}]} \quad (2)$$

$$\text{OT } (^\circ\text{C}) = 14.38 \times \text{TEX}_{86}^L + 8.93; \text{ with a calibration error of } \pm 0.6^\circ\text{C} \quad (3)$$

237 The OH-GDGT-based index, RI-OH' (Eq 4) and the OT estimation (Eq 5) were determined following Lü
 238 et al. (2015). In their study, they determined that the RI-OH' is significantly correlated with temperature
 239 compared to other indices such as TEX_{86} and RI-OH, producing a lower and less scattered residual sea
 240 surface temperature (SST) of $\pm 6^\circ\text{C}$.

$$\text{RI-OH}' = \frac{[\text{OH-GDGT-1}] + 2 \times [\text{OH-GDGT-2}]}{[\text{OH-GDGT-0}] + [\text{OH-GDGT-1}] + [\text{OH-GDGT-2}]} \quad (4)$$

$$\text{RI-OH}' = 0.0382 \times \text{OT } (^\circ\text{C}) + 0.1 \quad (R^2 = 0.75, n = 107, p < 0.01) \quad (5)$$

241 The index of relative contribution of terrestrial organic matter against that of marine input (branched-
 242 isoprenoid tetraether, BIT; Eq 6) was calculated based on Hopmans et al. (2004):

$$\text{BIT} = \frac{[\text{brGDGT-I}] + [\text{brGDGT-II}] + [\text{brGDGT-III}]}{[\text{Crenarchaeol}] + [\text{brGDGT-I}] + [\text{brGDGT-II}] + [\text{brGDGT-III}]} \quad (6)$$

243 Lastly, we utilize the ring index (RI; Eqs 7 - 9; Zhang et al., 2016) and methanogenic source indicator
 244 index (%GDGT-0; Eq 10; Inglis et al., 2015) to validate against possible non-thermal GDGT sources
 245 contribution:

$$\text{RI}_{\text{sample}} = 0 \times [\text{isoGDGT-0}] + 1 \times [\text{isoGDGT-1}] + 2 \times [\text{isoGDGT-2}] + 3 \times [\text{isoGDGT-3}] + 4 \times [\text{crenarchaeol}] + 4 \times [\text{regio. crenarchaeol}] \quad (7)$$

$$\text{RI}_{\text{calculated}} = -0.77 \times \text{TEX}_{86} + 3.32 \times (\text{TEX}_{86})^2 + 1.59 \quad (8)$$

$$|\Delta\text{RI}| = \text{RI}_{\text{calculated}} - \text{RI}_{\text{sample}} \quad (9)$$

$$\% \text{isoGDGT-0} = \frac{[\text{isoGDGT-0}]}{[\text{isoGDGT-0}] + [\text{Crenarchaeol}]} \times 100\% \quad (10)$$

246 3.3 Diatom analyses

247 41 smear slides were prepared for a quantitative diatom assemblage analysis at respective depths
 248 of the core. Between 400-600 diatom valves, inclusive of those from *Chaetoceros* resting spores
 249 (*Chaetoceros* rs), were counted in each sample to ensure statistical significance of the results. Diatoms
 250 were identified to species or species group level and, if possible, to forma or variety level. The presence
 251 of sea ice is inferred from the percentage of sea-ice indicating diatoms. A combined relative abundance
 252 of *Fragilariopsis curta* and *Fragilariopsis cylindus* (hereon referred to as *F. curta* gp) of >3% is used as
 253 a qualitative threshold to represent presence of WSI, while values between 1 and 3% estimates the

254 edge of maximum winter sea ice (Gersonde et al., 2003; 2005). Likewise, *Fragilariopsis obliquecostata*
255 is used to indicate summer sea ice (Gersonde and Zielinski, 2000).

256 We reconstructed WSI concentration (WSIC) by applying a marine diatom transfer function
257 developed by Esper and Gersonde (2014b; TF MAT-D274/28/4an). This transfer function consists of
258 274 reference samples from surface sediments in the Atlantic, Pacific and western Indian sectors of the
259 SO, with 28 diatom taxa and taxa groups, and an average of 4 analogs (Esper and Gersonde, 2014b).
260 The WSI estimates refer to September sea-ice concentration averaged over a period between 1981
261 and 2010 at each surface sediment site (National Oceanic and Atmospheric Administration, NOAA;
262 Reynolds et al., 2002; 2007). The reference dataset fits our approach as it uses a 1° by 1° grid, providing
263 a higher resolution than previously used, and giving a root mean square error of prediction of 5.52%
264 (Esper and Gersonde, 2014b).

265 The SSST was estimated using TF IKM-D336/29/3q (standard error of $\pm 0.86^\circ\text{C}$), comprising 336
266 reference samples from surface sediments in the Atlantic, Pacific and western Indian sectors of the SO,
267 with 29 diatom taxa and taxa groups, and a 3-factor model calculated with quadratic regression (Esper
268 and Gersonde, 2014a). The SSST estimates refer to summer (January-March) temperatures at 10 m
269 water depth averaged over a time period from ≤ 1900 to 1991 (Hydrographic Atlas of the Southern
270 Ocean; Olbers et al., 1992). The Hydrographic Atlas of the Southern Ocean was used because it
271 represents an oceanographic reference dataset least influenced by the recent warming in the SO (Esper
272 and Gersonde, 2014a).

273 **3.4 Comparison with other proxy records**

274 The EDML ice core and the marine sediment core PS67/219-1 are used in this study for regional
275 comparison due to proximity of both cores to our core site (Fig. 1a; see also Table 1 for details). Water
276 isotope ($\delta^{18}\text{O}$) and ssNa^+ records of the EDML ice core were investigated by EPICA Community
277 Members (2006) and Fischer et al. (2007), respectively. Marine sediment core PS67/219-1, retrieved
278 from the South Scotia Sea, is located south of the Polar Front and just north of the modern-day winter
279 sea-ice extent. This core offers data on sea ice, SSST and biogenic opal, which extend at least to the
280 LIG period, making it suitable for comparison with core site PS118_63-1. The chronology and biogenic
281 opal data of core PS67/219-1 was described and published in Xiao et al. (2016b), while investigations
282 on sea-ice reconstruction and SSST for the last 30 ka BP are presented in Xiao et al. (2016a). We
283 further extend the WSIC and SSST records, back to 150 ka BP, using the transfer functions TF MAT-
284 D274/28/4an and TF IKM-D336/29/3q, respectively (Esper and Gersonde, 2014b; 2014b).

285 **3.5 Comparison with simulations from climate model(s)**

286 Here, we also analyze model-simulated sea ice, SST and OT estimates for further comparison and
287 evaluation against our proxy results. In this respect, the strength of our modeling approach is twofold.
288 First, the model shall provide reasonable coverage of our intended studied time slices, mainly 6, 21,
289 125, 128 and 140 ka BP. Second, the model's sensitivity to various climate forcings and boundary
290 conditions across the Quaternary and the entire Cenozoic era must be known. To this end, the
291 Community Earth System Models (COSMOS; Jungclauss et al., 2006) is chosen over other climate

292 models due to its proven track record. For example, the simulation ensemble that has been produced
293 over the years with COSMOS is extensive and not available from international modeling initiatives like
294 the Paleoclimate Modeling Intercomparison Project (PMIP; e.g., Braconnot et al., 2012). Likewise, the
295 model has reproduced various aspects of reconstructed paleoclimate data (see Supplement S3.1 for a
296 list of paleo-studies using the COSMOS model), is shown to be sensitive to paleogeography and climate
297 forcing, and is being characterized by a large Climate and Earth System Sensitivity (Haywood et al.,
298 2013; Stepanek and Lohmann, 2012). Additionally, COSMOS has been proven useful for the study of
299 both warmer (Pfeiffer and Lohmann, 2016) and colder (Zhang et al., 2013; 2017) climates than today
300 and supported research in sometimes very interdisciplinary frameworks (e.g., Guagnin et al., 2016;
301 Klein et al., 2023). For some of the periods relevant here – Holocene, Last Glacial Maximum, LIG –
302 standalone applications of the model are documented (e.g., Pfeiffer and Lohmann, 2016; Wei and
303 Lohmann, 2012; Zhang et al., 2013). More importantly, results from COSMOS have been extensively
304 compared to other models, particularly within the framework of the PMIP, with a focus on the
305 Holocene (Dallmeyer et al., 2013; 2015; Varma et al., 2012) and the Last Interglacial (Bakker et al.,
306 2014; Jennings et al., 2015; Lunt et al., 2013). A relevant inference from comparing PMIP3-class models
307 is that, from the viewpoint of model performance in the SO, COSMOS has shown to be among the
308 models with a comparably minor warm bias in SST (see Fig. 4e and f in Lunt et al., 2013). This makes
309 COSMOS particularly suitable for the studies of ocean temperatures and sea ice around the Weddell
310 Sea. We refer to additional discussion on the rationale for choosing COSMOS over the PMIP models
311 in our study in the Supplement S3.3. Additionally, we also provide an in-depth comparison and
312 evaluation of the simulated results from PMIP3 and PMIP4 ensemble models, within the context of our
313 study, and agreement between COSMOS and PMIP ensemble models in the Supplement S3.4.

314 3.5.1 *Community Earth System Models*

315 In our study, the model data is derived from climate simulations performed with COSMOS. The
316 model's atmospheric module is the fifth generation of the European Centre for Medium-Range Weather
317 Forecasts' Model (ECHAM5), a model of the general circulation of the atmosphere, with a spectral
318 dynamical core, developed at the Max Planck Institute for Meteorology in Hamburg up to the sixth
319 generation (Stevens et al., 2013). In our model setup, the ECHAM5 is employed at a truncation of T31,
320 corresponding to a spatial resolution of approximately $3.75^\circ \times 3.75^\circ$, or 400 km at the equator. The
321 atmospheric column is discretized at a resolution of 19 vertical hybrid sigma-pressure levels. The
322 ECHAM5 also encompasses a land surface component (JSBACH) that represents multiple land cover
323 classification types (Loveland et al., 2000; Raddatz et al., 2007). We employ JSBACH's capability to
324 reflect vegetation dynamics (Brovkin et al., 2009) in the course of climate simulations. In our setup, we
325 consider eight different plant functional types (see Table 1 in Stepanek and Lohmann, 2012) that the
326 model adapts in response to changes in the simulated climate, thereby reflecting important feedback
327 processes between vegetation and climate in our simulations (Stepanek et al., 2020). The ocean
328 module is the Max Planck Institute Ocean Model (MPIOM; Marsland et al., 2003), employed at 40
329 unevenly spaced pressure levels with a bipolar curvilinear GR30 grid that has a formal resolution of
330 $1.8^\circ \times 3.0^\circ$. This enables the horizontal resolution to reach grid cell dimensions that are as small as 29

331 km at high latitudes. Sea ice computation is based on dynamic-thermodynamic processes with viscous-
332 plastic rheology and follows the formulation by Hibler (1979). Various parameterizations improve the
333 representation of small-scale ocean dynamics in the simulations. For additional information about the
334 parameterizations utilized in our model setup, and for the steps taken to create geographic setups to
335 apply the model in paleoclimatological research, see, for example, Stepanek et al. (2020) and
336 references therein.

337 3.5.2 COSMOS simulation settings

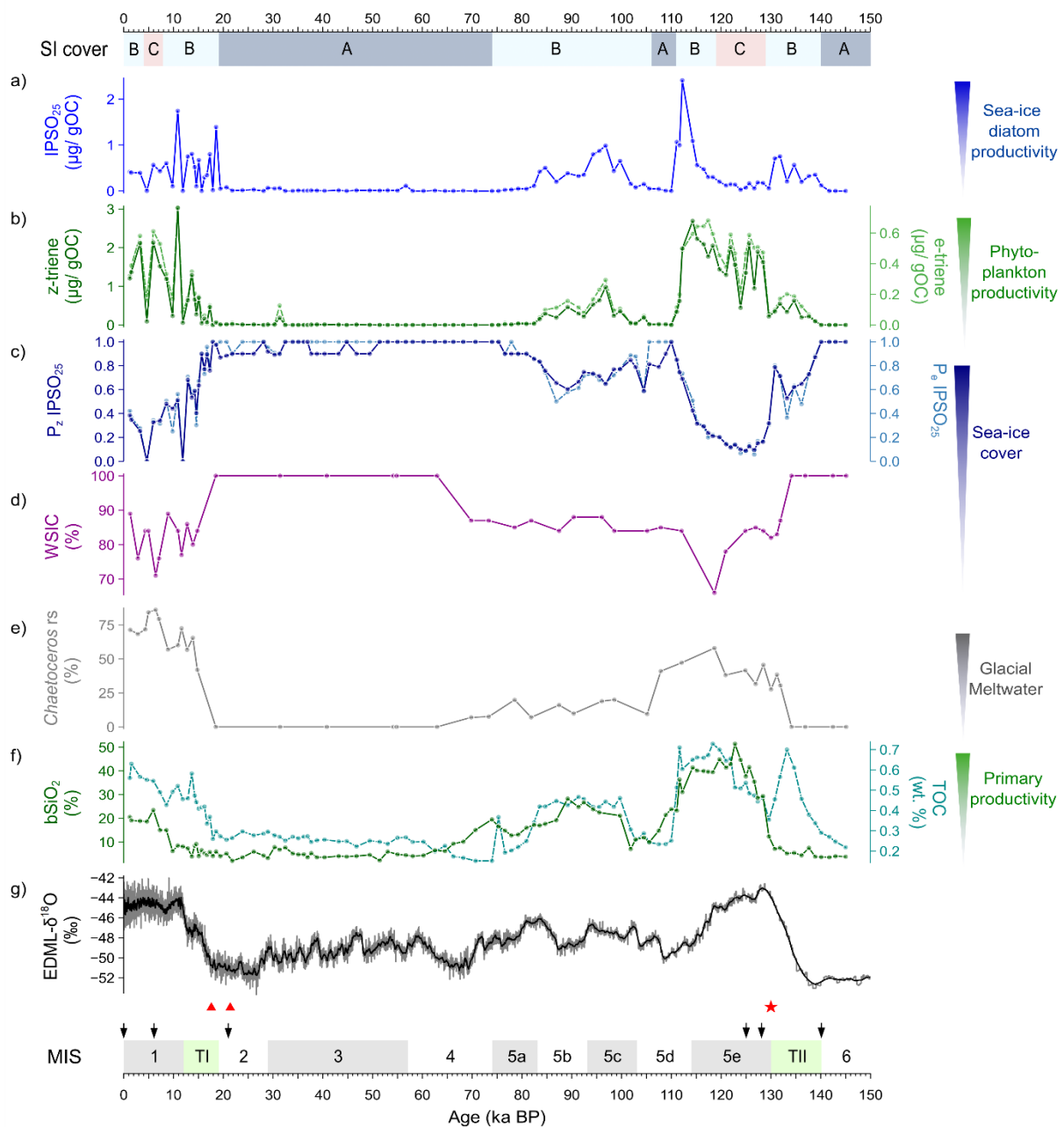
338 The simulation ensemble consists of a pre-industrial reference state (simulation *piControl*, 1850
339 CE; Wei and Lohmann, 2012), a mid-Holocene climate (simulation *mh6k*, 6 ka BP; Wei and Lohmann,
340 2012), an LGM state (simulation *lgm21k*, 21 ka BP; Zhang et al., 2013), two time-slices of the LIG,
341 where one refers to conditions at 125 ka BP (simulation *lig125k*) and one to conditions at 128 ka
342 (simulation *lig128k*), and a Penultimate Glacial Maximum (PGM) climate (simulation *pgm140k*). In order
343 to filter out short-term climate variability on interannual and multidecadal time scales, and to derive
344 average climatic conditions that are representative of the respective Quaternary time-slice, we average
345 the modeled climate state over a period of 100 model years. For interglacial climates we employ a
346 modern geography. The boundary conditions for the Last and Penultimate Glacial Maximum have been
347 set up for a study by Zhang et al. (2013) based on the PMIP3 modeling protocol. Details of the ice-
348 sheet reconstruction, that is a blend of ICE-6G v2.0 (Argus and Peltier, 2010), ANU (Lambeck et al.,
349 2010) and GLAC-1a (Tarasov et al., 2012), are described by Abe-Ouchi et al. (2015). For further details
350 on the climate states and simulation configurations, we refer to the supplement (S3.2 and
351 Supplementary Table S3, respectively). For analysis, the climate model output is interpolated from the
352 native grid of the ocean model to a regular resolution of 0.25°x0.25°. High resolution is chosen in order
353 to preserve the geographic features of the ocean model. Additionally, we also derived climate model
354 data specifically tailored to the two marine core sites discussed in this paper, achieving this through
355 interpolating relevant climate fields to the geographic coordinates of each core using a nearest-neighbor
356 interpolation algorithm. Any reference to the modeled sea-ice edges in this publication specifies the
357 isoline of 15% of sea-ice cover.

358 4 Results

359 4.1 HBIs

360 The concentration of the sea-ice biomarker (IPSO₂₅; Fig. 3a) in core PS118_63-1 varies
361 significantly between 0 and 2.41 µg/g OC. Peak concentration is found at ca. 112 ka BP, while very low
362 concentrations are noted throughout MIS 2-4, 5d, 5e and 6. Moderate to low concentrations are
363 observed during MIS 1 and through both terminations. The concentration of the ice marginal-open water
364 phytoplankton biomarkers varies between 0 - 3.03 µg/g OC (z-triene) and 0 - 0.76 µg/g OC (e-triene;
365 Fig. 3b). Higher concentrations are observed at MIS 1 and 5e, while lower concentrations are noted
366 throughout MIS 2-4, 5d and 6. In our investigation, we utilized both z- and e-trienes, respectively, to
367 calculate the semi-quantitative spring/summer sea-ice indices (P_{z/e}IPSO₂₅). This combined use of

368 biomarkers, indicative of ice marginal-open water conditions and $IPSO_{25}$, helps to circumvent
 369 ambiguous interpretations especially when dealing with scenarios of permanent sea ice and open ocean
 370 conditions. Our $P_z IPSO_{25}$ index ranges between 0.09 and 1, while the $P_e IPSO_{25}$ index varies from 0.06
 371 to 1 (Fig. 3c). Instances, where both values of $IPSO_{25}$ and z-/e-triene are zero, the $P_{z/e} IPSO_{25}$ index is
 372 assigned a value of 1, indicating permanent ice cover. Both index profiles presented a similar trend (r
 373 = 0.98), with higher values (>0.8) throughout MIS 2-4, 5d and 6, while reduced values are noted for MIS
 374 1 and 5e. Notably, the lowest $P_{z/e} IPSO_{25}$ values (<0.2) are observed during MIS 5e, specifically between
 375 119 and 128 ka BP, signifying a distinct decline in sea ice and more open ocean conditions during this
 376 time interval. Comparable low $P_{z/e} IPSO_{25}$ values are also observed around 4 and 12 ka BP.



377

378 **Figure 3. Multiproxy analyses of sea-ice conditions in Powell Basin, reconstructed from marine sediment**
 379 **core PS118_63-1. Sea-ice (SI) cover scenarios: A - permanent sea-ice cover (dark blue), B - dynamic sea-**
 380 **ice cover (light blue) and C - minimal sea-ice cover (light red). From top to bottom: a) HBI-based sea ice**
 381 **biomarker ($IPSO_{25}$), b) HBI-based phytoplankton biomarkers (z-/e-trienes), c) Phytoplankton- $IPSO_{25}$ index**

382 (PIPSO₂₅), d) Diatom-based winter sea-ice concentration (WSIC), e) Glacial meltwater indicator
383 (*Chaetoceros* resting spores) and f) Biogenic opal (bSiO₂), and total organic carbon (TOC). Atmospheric
384 temperature is implied by g) the δ¹⁸O record from the EDML ice core. AMS ¹⁴C dates are marked with red
385 triangles, the biostratigraphic marker (*R. leventerae*) is indicated by the red star. The black arrows
386 delineated the time-slices for the model simulations in this study. MIS stages are depicted in alternating
387 grey (odd) and white (even) shades, while the terminations TI and TII are shown in green.

388 4.2 GDGTs

389 Downcore OT estimates using the RI-OH' index cover a temperature range between -2.5 and
390 1.0°C (Fig. 4g) while TEX₈₆^L-derived OT fluctuates between -2.6 and 1.0°C (Supplementary Fig. S5a).
391 These GDGT-based OTs likely reflect (mean) annual ocean temperature between the water depths of
392 0 and 200 m (Hagemann et al., 2023; Kim et al., 2012; Liu et al., 2020), and this seems to be
393 corroborated by the modern-day vertical ocean temperature profile nearby core site PS118_63-1 (Fig.
394 1b). Certainly, these minimum temperatures of less than -1.9°C – freezing temperature of seawater –
395 need to be considered with caution due to factors influencing the ocean temperature calibration, for
396 example, bias from terrestrial input, water depth, use of satellite-assigned ocean temperature below the
397 freezing point of seawater and inadequate samples from polar areas (Fietz et al., 2020; Xiao et al.,
398 2023). Nevertheless, both OT proxies consistently indicate a cold-water subsurface regime (0 – 200 m;
399 <1°C) with a 0-2°C temperature fluctuation, and no significant glacial/interglacial variability over the last
400 145 kyrs. We further note that the RI-OH'-based OTs fluctuate within the error range of the temperature
401 calibration based on a global surface sediment dataset (Lü et al., 2015) and call for attention when
402 interpreting OT variability. Calculation of terrestrial originated-GDGT (i.e. BIT) and isoGDGT-related
403 indices (i.e. %isoGDGT-0 and ΔRI; Supplementary Fig. S5b-e) reveals the presence of potential non-
404 thermal influences on the TEX₈₆^L index, which may lead to bias in the temperature reconstruction (see
405 also S4 in the Supplement). In light of the non-thermal influences on TEX₈₆^L, we have decided not to
406 further discuss on the TEX₈₆^L-derived OT in this paper. Concerning the RI-OH' approach, the presence
407 of OH-GDGT has, thus far, only been observed within the cultivated marine thaumarchaeal group I.1a
408 (Pitcher et al., 2011; Liu et al., 2012b; Elling et al., 2014; 2015). Its absence in the terrestrial
409 thaumarchaeal group I.1b (Sinninghe Damsté et al., 2012) suggests a predominantly planktic origin (Lü
410 et al., 2015). While both isoGDGTs and OH-GDGTs are derived from the phylum *Thaumarchaeota*,
411 variances in their ring composition indicate that the OH-GDGTs may be biosynthesized from different
412 source organisms or differing conditions (Liu et al., 2012b). Additionally, previous studies compared the
413 relationship between various GDGT-based indices (i.e. RI-OH, RI-OH', TEX₈₆ and TEX₈₆^L) and
414 temperature, and determined that the RI-OH'-temperature relationship shows the most significant
415 correlation in cold-water (<15°C) regions, making the RI-OH' a robust temperature proxy for the
416 (sub)polar regions (Lü et al., 2015; Lamping et al., 2021; Park et al., 2019; Fietz et al., 2020). Therefore,
417 we suggest that the RI-OH' index holds promise as a potential OT proxy for our study site. However,
418 further work on the distribution of OH-GDGT and calibration studies are still essential to enhance the
419 applicability of RI-OH' as a (paleo)temperature proxy.

420 4.3 Diatoms

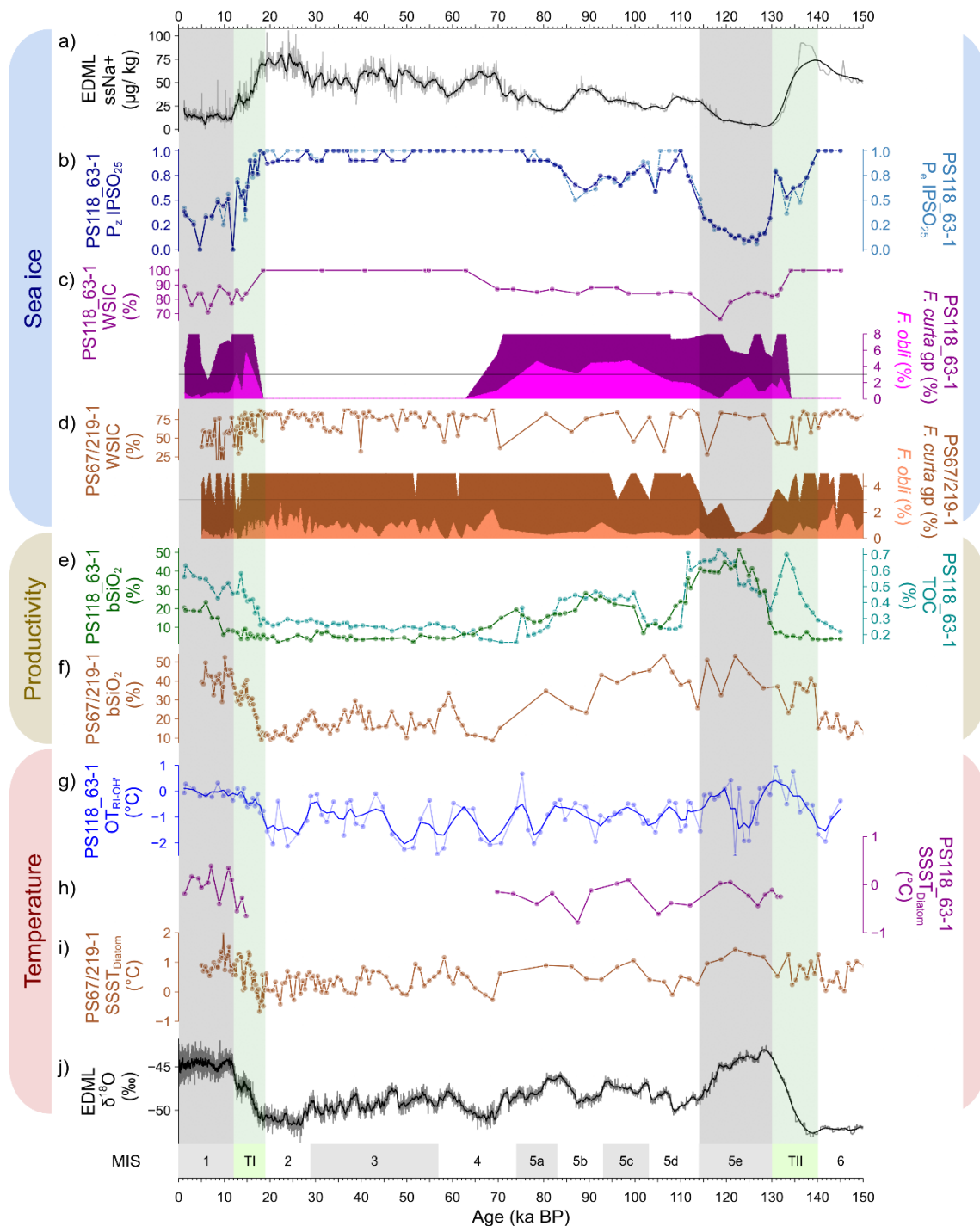
421 The diatom-based data for cores PS118_63-1 and PS67/219-1 are presented in Fig. 4c and d. For
422 core PS118_63-1 from the Powell Basin, the relative abundance of sea ice-related diatoms ranges

423 between 2 and 39% for *F. curta* gp, and from 0 to 6% for *F. obliquocostata*. The relative abundance of
424 diatoms between ca. 15 and 70 ka BP, and before 131 ka BP, is rare/absent (Fig. 4c). Such cases
425 generally indicate the presence of permanent sea ice over the core site (Zielinski and Gersonde, 1997).
426 We, therefore, assign the diatoms' relative abundance as 0, and WSIC as 100%, to above-mentioned
427 time intervals (i.e., MIS 2 - 4 and 6). The abundance of *F. curta* gp is noted to be above the 3% threshold
428 (indicative of presence of WSI) throughout the remaining time periods – except at 6 ka BP, where the
429 lowest abundance (2%) is observed. A relative abundance of *F. obliquocostata* around the 3% threshold
430 indicates a dynamic summer sea-ice edge over the area during MIS 1 and 5. The WSIC across the rest
431 of the time frame, namely MIS 1 and 5, is generally high (>75%) with a couple of lower WSIC observed
432 at ca. 6 ka BP (71%) and at 119 ka BP (66%). The abundance of *Chaetoceros* resting spores
433 (*Chaetoceros* rs) varies between 0 and 86%, with higher values noted during MIS 1 and 5e (Fig. 3e).
434 Such increases in the abundance of the *Chaetoceros* rs imply the presence of glacial meltwater at the
435 core location (Crosta et al., 1997). The diatom-derived SSST – typically indicating summer ocean
436 temperature between the water depth of 0 and 10 m – covers a temperature range between -0.8 and
437 0.4°C (Fig. 4h), and describes a cold-water region during MIS 1 and 5, similar to the RI-OH'-derived OT
438 (Fig. 4g).

439 To the north in the South Scotia Sea, core PS67/219-1 documents an overall lower percentage of
440 sea ice-related diatoms (Fig. 4d). Similar to core PS118_63-1, the relative abundance of *F. curta* gp
441 (0.5-20%) is noted to be mostly above the 3% threshold, indicating presence of WSI over the region,
442 with higher abundance observed for MIS 2 and 3, and lowest abundance (<1%) observed during MIS
443 5e. However, the relative abundance of *F. obliquocostata* for core PS67/219-1 remains below the 3%
444 threshold, between 0 and 3%, suggesting a lack of summer sea ice over the core site. The percentage
445 of WSIC in the South Scotia Sea is also lower than that of Powell Basin, with a record of 37-82%. The
446 diatom-based SSST documents a SSST range of -0.7 to 2°C, with colder SSST registered during MIS
447 2 and 3, and warmer SSST noted during MIS 1 and 5e (Fig. 4i).

448 **4.4 TOC and Biogenic opal**

449 In this study, both TOC and biogenic opal (Fig. 3f) are interpreted to reflect primary productivity (r
450 = 0.65). The TOC content varies between 0.2 and 0.7% while biogenic opal ranges from 2 to 51%.
451 Highest productivity is observed during MIS 1 and 5e, indicative of favorably warmer conditions that
452 promote primary productivity blooms at the core location. A rather moderate productivity level is
453 observed between MIS 5a to c, while lowest values are noted for MIS 2-4, 5d and 6. Both profiles also
454 exhibit some differences. For example, peak biogenic opal occurs around 124 ka BP whilst peak TOC
455 is recorded at 119 ka BP. We also observe a more pronounced increase in the TOC content during the
456 terminations than in the biogenic opal content. This is likely due to greater input from non-siliceous
457 organisms, such as archaeal, bacterial and terrestrial input (see Supplementary Fig. S4).



458

459 **Figure 4. Regional sea ice, productivity and temperature variability in the South Atlantic sector of the**
 460 **Southern Ocean as inferred from EDML ice core, Powell Basin (PS118_63-1) and South Scotia Sea**
 461 **(PS67/219-1). For sea ice: a) sea-ice estimation (ssNa+; black) from EDML ice core, b) HBI-based sea ice**
 462 **indicator (P_zIPSO₂₅ – dark blue; P_eIPSO₂₅ – dotted light blue), c) diatom-based winter sea-ice concentration**
 463 **(WSIC – dark magenta), *F. curta* gp (dark magenta), *F. obliquocostata* (*F. obli* – light**
 464 **465 magenta) from PS118_63-1, and d) diatom-based WSIC (brown), *F. curta* gp (*F. curta* gp – brown), *F.*
 466 ***obliquocostata* (*F. obli* – light brown) from PS67/219-1. For productivity: e) biogenic opal (bSiO₂ – dark**
 467 **green) and total organic carbon (TOC – dotted light green) from PS118_63-1 and f) bSiO₂ (brown) from**
 468 **PS67/219-1. For temperature: g) RI-OH'-derived subsurface ocean temperature with three-point smoothing**
 469 **(OT_{RI-OH'} – navy blue) and h) summer sea surface temperature (SSST_{Diatom} – dark magenta) from PS118_63-**
 470 **1, i) SSST_{Diatom} (brown) from PS67/219-1 and j) EDML water stable isotope record (δ¹⁸O – black). The 3%**
 471 **threshold for diatom species relative abundance is indicated by a black horizontal line. MIS stages are**
 472 **depicted in alternating grey (odd) and white (even) shades, while the terminations TI and TII are shown in**
 473 **green. For the full *F. curta* gp abundance data, refer to the relevant datasets in Pangaea (refer to Data**
 474 **availability).****

474 **4.5 Sea-ice conditions – a multiproxy approach**

475 Using a multiproxy approach, our analysis of the data from core PS118_63-1 provides a
476 continuous glacial-interglacial sea-ice history in the Powell Basin since the PGM. We distinguish three
477 different sea-ice scenarios spanning the last 145 kyrs (Fig. 3).

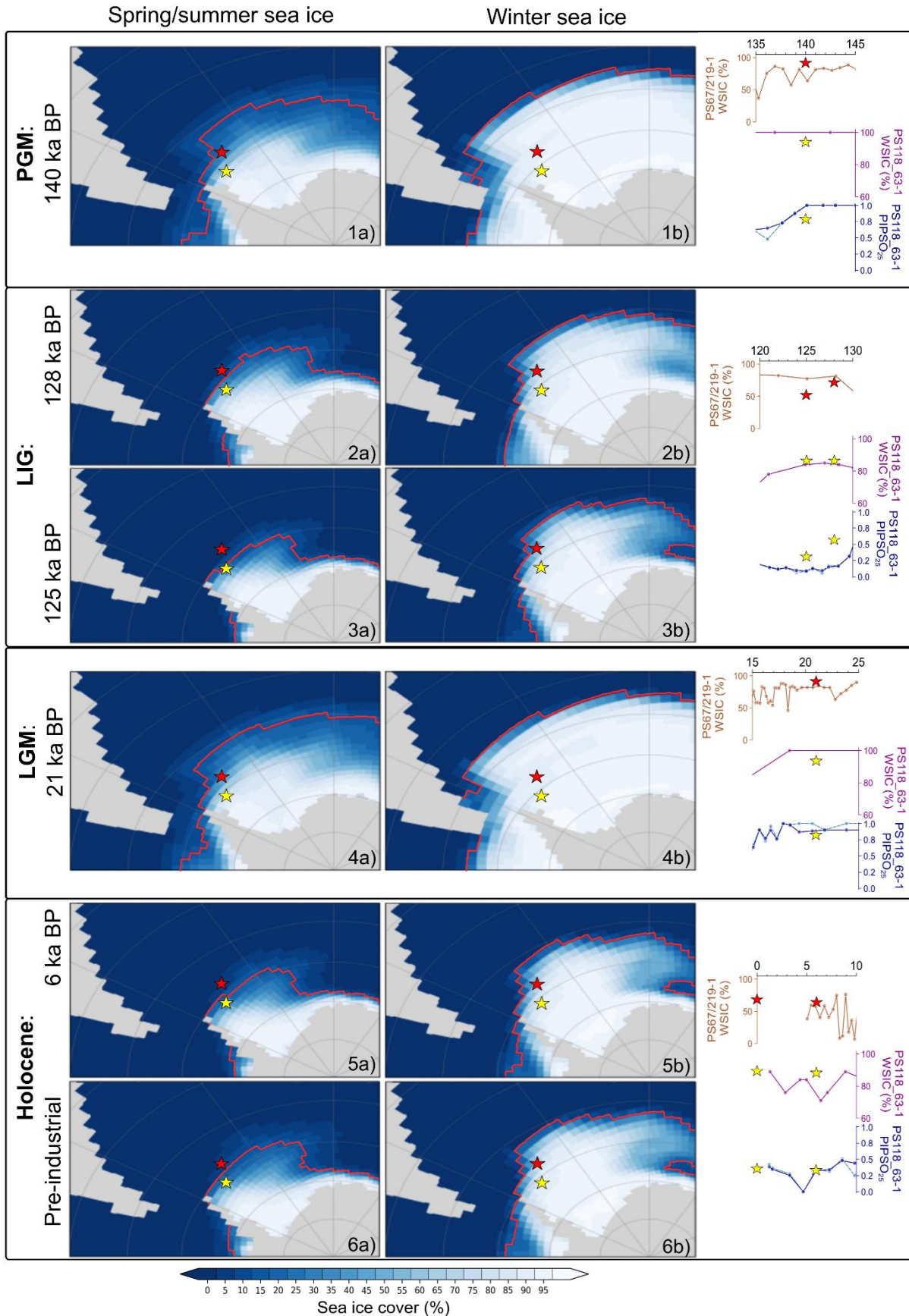
478 *A) Perennial sea-ice cover.* This scenario is characterized by remarkably low (sea ice) diatom
479 abundances, minimum IPSO₂₅ and HBI-triene concentrations, as well as minimum bSiO₂ and TOC
480 contents. We deduce the presence of maximum WSIC and spring/summer sea ice (PIPSO₂₅)
481 cover. These results indicate a glacial setting, with our core site situated under a perennial sea ice
482 or ice-shelf cover suppressing primary production in the water column. Such a scenario persisted
483 throughout the glacial periods MIS 2-4, MIS 6, and during MIS stadial 5d.

484 *B) Dynamic sea-ice cover.* This scenario is described by fluctuations in each of the proxy profiles,
485 in particular WSIC, PIPSO₂₅, HBI-trienes, bSiO₂ and TOC contents. These records reflect the
486 dynamic nature of sea-ice conditions over our core site, with varied primary production at different
487 time intervals. This scenario is prevalent during periods of climate transition, such as terminations
488 I and II, and during MIS 1 and 5a-c.

489 *C) Minimal (winter-only) sea-ice cover.* This scenario is denoted by a considerably reduced sea-
490 ice diatom (IPSO₂₅) production, WSIC and PIPSO₂₅, coupled with high phytoplankton productivity
491 (HBI-trienes), bSiO₂ and TOC contents. These findings suggest that our core site experienced ice-
492 free or winter-only ice conditions, permitting enhanced primary production in the water column.
493 This scenario occurs in short time intervals within the MIS 1 and MIS 5e.

494 **4.6 Inferences from COSMOS simulations**

495 Covering the Atlantic sector of the SO, our model-simulated sea ice, SST and OT (at 220 m water
496 depth) glacial-interglacial time-slices cover the PGM at 140 ka BP, LIG at 128 (sea ice only) and 125
497 ka BP, LGM at 21 ka BP, Holocene at 6 ka BP and pre-industrial (Fig. 5 - 7). In Fig. 5, the left column
498 (Fig. 5a) shows the simulated sea-ice cover/extent for the spring/summer seasons (NDJFMA, this
499 averaging period considers the time lag in sea-ice extent vs. spring/summer temperature evolution)
500 while the right column (Fig. 5b) illustrates the simulated sea-ice cover/extent for the winter (ASO)
501 season. In general, a greater sea-ice cover is observed during winter than spring/summer for each time-
502 slice. During the glacial periods, the model highlights a northward expansion of the sea-ice extent
503 beyond both marine core sites (PGM: Fig. 5.1; LGM: Fig. 5.4). At the more southern site (Powell Basin;
504 core PS118_63-1), the modeled glacial sea-ice cover varies between ~93 to 94% (winter) and ~79 to
505 82% (spring/summer), while at the more northern site (South Scotia Sea; core PS67/219-1), sea-ice
506 cover varies around ~91% (winter) and ~26 to 34% (spring/summer). In contrast, during the
507 interglacials, fluctuations in sea-ice extent are more pronounced between seasons. WSI extent is
508 observed to be located north of both core sites (Fig. 5.2b, 5.3b, 5.5b and 5.6b), with the WSI cover
509 ranging between ~86 and 89% at core site PS118_63-1, and ~52 to 69% at core site PS67/219-1.
510 During spring/summer, the sea-ice extent retreats to a latitude between both sites (Fig. 5.2a, 5.3a, 5.5a
511 and 5.6a), with the spring/summer sea-ice cover varying from ~31 to 35% at core site PS118_63-1 and
512 between ~0 and 4% at core site PS67/219-1.



513

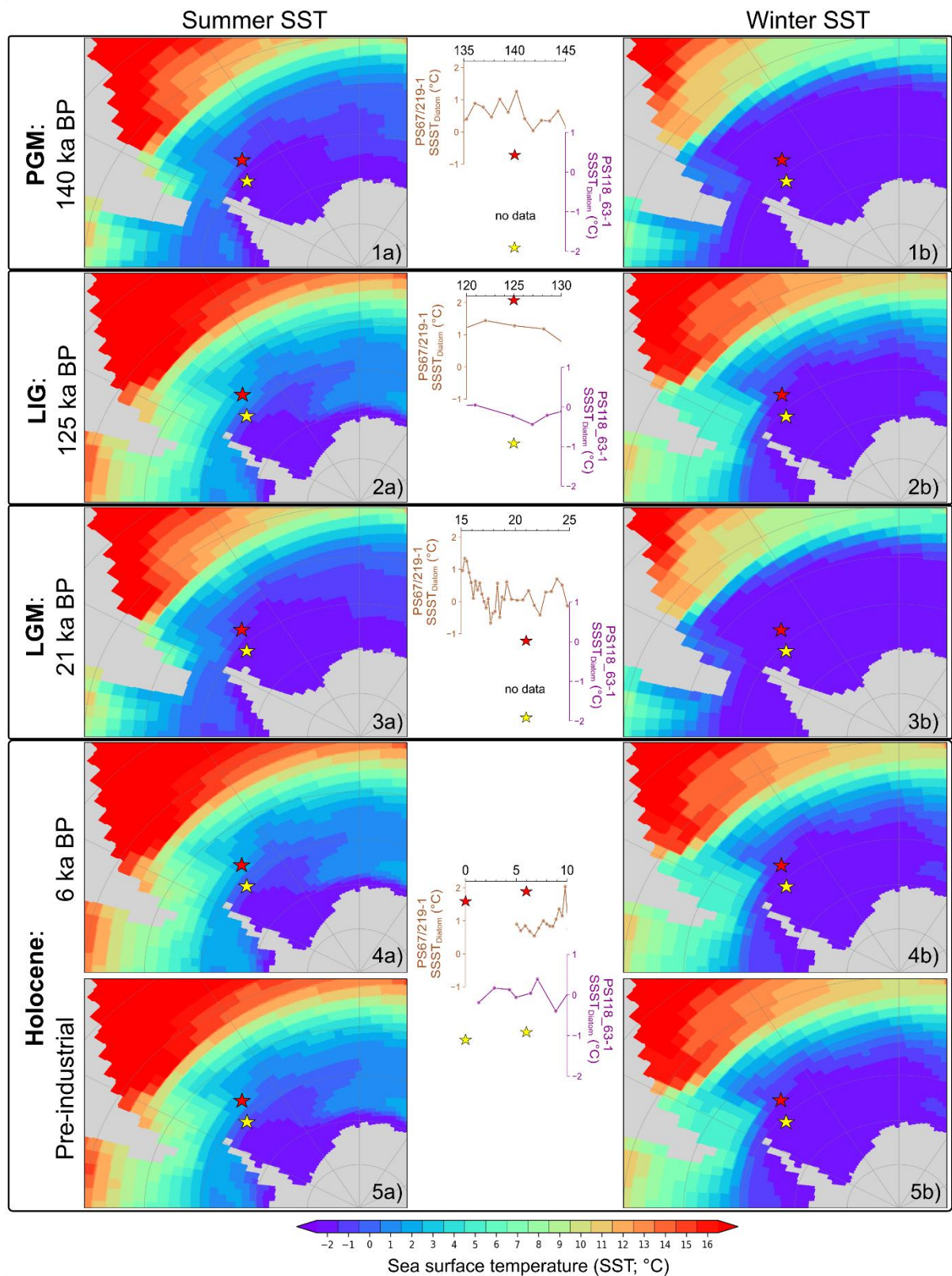
514

515

516

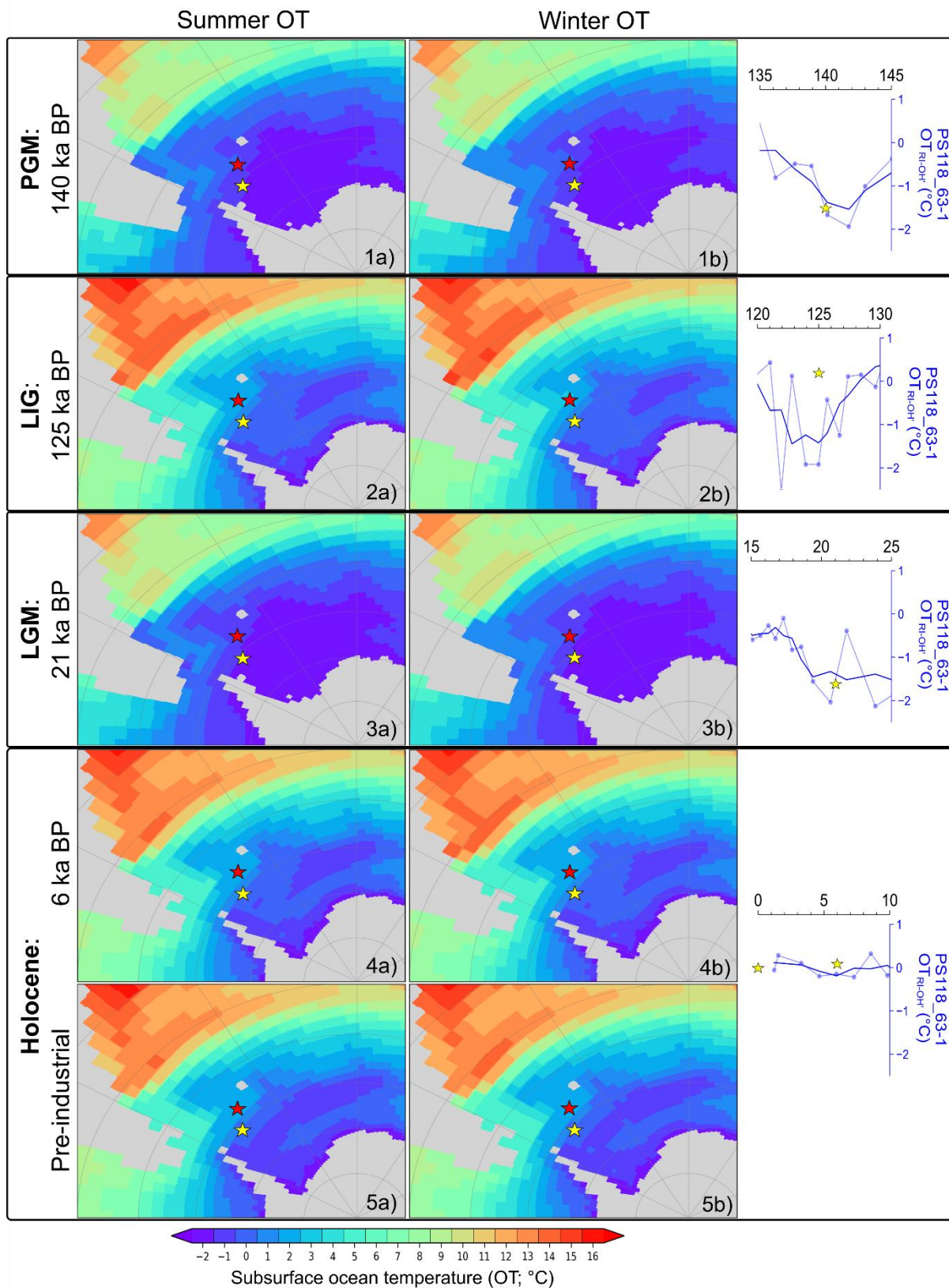
Figure 5. Model-simulated mean a) spring/summer (NDJFMA) and b) winter (ASO) sea-ice cover for the various time slices: 1) PGM: 140 ka BP, 2) LIG: 128 ka BP, 3) LIG: 125 ka BP, 4) LGM: 21 ka BP, 5) mid-Holocene: 6 ka BP and 6) Pre-industrial. The red line depicts the sea-ice extent and is defined as the isoline

517 of 15% sea ice coverage. Locations of marine sediment cores are indicated by stars: PS118_63-1 (yellow)
 518 and PS67/219-1 (red). Proxy-derived winter sea-ice concentration (WSIC) and spring/summer sea ice
 519 (PIPSO₂₅) at each core location are shown in the right-most panel. Additionally, model-simulated sea-ice
 520 values at each core site (yellow and red stars) for each time slice are plotted alongside the proxy data for
 521 comparison.



522
 523 **Figure 6. Model-simulated mean a) summer (DJF) and b) winter (JJA) sea surface temperature (SST) for**
 524 **the various time slices: 1) PGM: 140 ka BP, 2) LIG: 125 ka BP, 3) LGM: 21 ka BP, 4) mid-Holocene: 6 ka BP**

525 and 5) Pre-industrial. Marine sediment cores, PS118_63-1 (yellow) and PS67/219-1 (red), are indicated by
 526 the colored stars. Diatom-based summer sea surface temperature (SSST_{Diatom}) at both core locations is
 527 presented in the middle panel. The corresponding model-simulated SST at each core site (yellow and red
 528 stars) for each time slice is displayed alongside the proxy data for comparison.



529
 530 **Figure 7. Model-simulated mean a) summer (DJF) and b) winter (JJA) subsurface ocean temperature (OT;**
 531 **220 m water depth) for the various time slices: 1) PGM: 140 ka BP, 2) LIG: 125 ka BP, 3) LGM: 21 ka BP, 4)**

532 mid-Holocene: 6 ka BP and 5) Pre-industrial. Marine sediment cores are presented in colored stars:
533 PS118_63-1 (yellow) and PS67/219-1(brown). Biomarker-based ocean temperature with three-point
534 smoothing (OT_{RI-OH}) for core PS118_63-1 is presented in the right panel. For comparison, the model-
535 simulated OT for core PS118_63-1 (yellow star) for each time slice are included alongside the proxy-derived
536 OT.

537 For the SST and OT, the left columns (Fig. 6a and 7a) represent the summer (DJF) temperature,
538 and the right columns (Fig. 6b and 7b) depict the winter (JJA) temperatures, respectively. The
539 simulated-SST (Fig. 6) appears similar to that of the modeled sea-ice output. In general, widespread,
540 low SST, close to the freezing point of seawater (that is approximately -1.9°C at salinity values modeled
541 in the SO in our simulations), is exhibited across all time-slices during winter (Fig. 6b), while in summer
542 (Fig. 6a), low SST mainly occurs in the Weddell Sea and along the coast of the Antarctic continent. For
543 instance, at the core site PS118_63-1 in Powell Basin, Weddell Sea, there is no observed difference in
544 SST between winter and summer during the glacial periods PGM (Fig. 6.1) and LGM (Fig. 6.3). Both
545 sites were surrounded by sea ice during these periods (Fig. 5.1 and 5.4). However, in interglacials, a
546 seasonal SST cycle of $\sim 1^{\circ}\text{C}$ is noted in the basin (Fig. 6.2, 6.4 and 6.5). In contrast, at the more northern
547 core site PS67/219-1, the model estimates a seasonal SST cycle of $\sim 1^{\circ}\text{C}$ during the glacial periods
548 (Fig. 6.1 and 6.3) and $\sim 3.4^{\circ}\text{C}$ during the interglacial (Fig. 6.2, 6.4 and 6.5). Moreover, the modeled
549 climate states are characterized by spatial SST gradients between the two core locations of between
550 0°C (glacial) and $\sim 0.4^{\circ}\text{C}$ (interglacial) during winter. For summer SST, the gradient between the two
551 core locations varies between $\sim 1^{\circ}\text{C}$ (glacial) and $\sim 2.8^{\circ}\text{C}$ (interglacial). As for the simulated OT, the
552 model displays a ~ 1.6 and $\sim 3^{\circ}\text{C}$ glacial-interglacial variation at core sites PS 118_63-1 and PS67/219-
553 1, respectively, but no appreciable OT change is observed between the winter and summer seasons of
554 each time slices (Fig. 7). The model also reveals a spatial OT gradient between both marine core sites
555 of $\sim 0.7^{\circ}\text{C}$ (glacial) and $\sim 2.1^{\circ}\text{C}$ (interglacial).

566 5 Discussion

567 5.1 Regional sea ice and oceanic conditions

568 5.1.1 Penultimate Glacial Maximum – Termination II

569 Our records show that during the PGM, the Powell Basin (core PS118_63-1) remained under a
570 layer of persistent (sea) ice cover, as evidenced by a 100% WSIC and peak PIPSO₂₅ values inferred
561 from the absence of diatoms, alongside notable reductions in IPSO₂₅ and HBI-triene concentrations
562 (see also Sect 4.1 and 4.3). This coincided with the lowest levels of primary production reflected in the
563 biogenic opal and TOC records (Fig 4b, c and e). This condition persisted until ca. 140 ka BP, when a
564 decline in spring/summer sea ice (PIPISO₂₅) is observed, accompanied by a rise in TOC and subsurface
565 ocean temperature (Fig. 4b, e and g). At a more northerly location in the South Scotia Sea, core
566 PS67/219-1 records a less pronounced sea-ice cover during the PGM with WSIC fluctuating at around
567 65% and a 1-3% abundance of *F. obliquocostata* suggesting the proximity of a permanent sea-ice edge
568 (Fig. 4d). These findings from the geological record are supported by our model simulation for the 140
569 ka BP time-slice, which shows an overall high simulated-WSI cover (94%; 92%), but slightly lower
570 simulated-spring/summer sea-ice cover (79%; 27%) at core sites PS118_63-1 and PS67/219-1,

571 respectively (Fig. 5a). Likewise, higher ssNa^+ concentrations and $\delta^{18}\text{O}$ values from EDML ice core point
572 to cold conditions and an extensive sea-ice cover in the Atlantic region (Fig. 4a and j; EPICA Community
573 Members, 2006; Fischer et al., 2007).

574 Termination II (TII; 140-130 ka BP) marks the transition from a glacial into an interglacial
575 environment. The onset of this deglaciation was probably initiated by a warming event caused by a
576 maximum southern high latitude summer insolation at around 138 ka BP (Bianchi and Gersonde, 2002;
577 Broecker and Henderson, 1998) and further sustained by the Heinrich Stadial 11 (HS11) event
578 occurring in the Northern Hemisphere (NH) between 135 and 130 ka BP (Turney et al., 2020). The
579 HS11 is a prominent North Atlantic meltwater event that may have triggered the eventual shutdown of
580 the AMOC, thus reinforcing the warming in the SO via the bipolar seesaw effect (Marino et al., 2015).

581 In the Powell Basin, the WSIC remains high (100%) and only starts to decrease (80%) at ca. 134
582 ka BP, while gradually declining PIPSO₂₅ values since 140 ka BP accompany the onset of the
583 deglaciation and mark a shift from a perennial sea ice to a dynamic seasonal sea-ice cover (see Sect
584 4.5 for definition). A concurrent rise in subsurface ocean temperature is also observed during this
585 timeframe. In contrast, core PS67/219-1 in the South Scotia Sea recorded a different sea-ice regime
586 with generally lower and declining WSIC and <1% abundance of *F. obliquocostata*, suggesting a less
587 extended sea-ice cover. The different sea-ice conditions in both regions are supported by a higher
588 biogenic opal production recorded in the South Scotia Sea as compared to the minimum biogenic opal
589 content observed for the Powell Basin (Fig. 4e and f). The Powell Basin TOC profile is also different
590 from its opal counterpart, with the former peaking between 135-131 ka BP. We surmise that this peak
591 may relate to a preferential growth environment for non-siliceous marine organisms and/or increased
592 input of terrestrial organic matter during this interval.

593 The persistent warming was interrupted by a short period of spring/summer sea ice (PIPISO₂₅) re-
594 expansion and weakened decline in WSI towards the end of TII (ca. 132-130 ka BP; Fig 4b and c),
595 along with an increasing *Chaetoceros RS* abundance that peaks at ca. 131 ka BP (Fig. 3e). These
596 conditions coincide with the northward shift of the sea-ice edge at ODP Site 1094 around 129.5 ka BP
597 (Bianchi and Gersonde, 2002). A comparable reduction in SSST at around 131 ka BP is also observed
598 in the South Scotia Sea (core PS67/219-1, Fig. 4i) and apparent at ODP Site 1089 and core PS2821-1
599 (Cortese and Abelman, 2002). In the Powell Basin, however, this cooling event is not reflected in
600 ocean temperature (Fig. 4g) and we propose that the lack of temperature change during this event may
601 be attributed to the discharge of meltwater from expanding sub-ice shelf cavities, which caused a
602 stronger stratification and an effective isolation of the warmer subsurface layer.

603 5.1.2 Last Interglacial - MIS 5 stadials/interstadials

604 Following the short-lived sea-ice expansion in Powell Basin at the end of TII, we observe a rapid
605 decline, and minimum spring/summer sea-ice cover is reached (see Sect 4.5) by ca. 129 ka BP (Fig.
606 4b). Lowest spring/summer sea ice (PIPISO₂₅) is observed between 126 and 124 ka BP, while minimum
607 WSIC is observed around 119 ka BP. These conditions promoted primary productivity, as reflected in
608 the maximum biogenic opal and TOC contents, at the respective timeframes (Fig. 4e). Likewise, sea
609 ice and temperature profiles from core PS67/219-1, the EDML ice core and model simulations also

610 favor a warm and predominantly open ocean condition for the South Atlantic sector throughout the LIG
611 (Fig. 4d, 4i, 5.3 and 6.3; EPICA Community Members, 2006; Fischer et al., 2007). Holloway et al.
612 (2017) investigated the simulated-spatial structure of the Antarctic WSI minimum at 128 ka BP with
613 respect to the $\delta^{18}\text{O}$ -isotopic peak recorded in the East Antarctic ice cores. They tested numerous WSI
614 retreat scenarios and concluded that the $\delta^{18}\text{O}$ maximum could be explained by a significant decline in
615 Antarctic WSI, with the Atlantic sector experiencing the largest reduction of 67%. Contrastingly, while
616 our spring/summer sea ice (PIPSO₂₅) data aligns with their $\delta^{18}\text{O}$ -accorded simulated-findings, our
617 diatom data - revealing a constant presence of WSI in the Powell Basin and South Scotia Sea with even
618 minor increases between 130 and 127 ka BP - disagrees. Furthermore, the WSI record from marine
619 core PS2305-6, located slightly north of our core site, also indicates the presence of WSI during MIS
620 5e (see also Supplementary Table S1 in Holloway et al., 2017; Bianchi and Gersonde, 2002; Gersonde
621 and Zielinski, 2000). We assume that the modeled winter sea-ice retreat seems to be valid for more
622 distal ocean areas, whereas at the core sites in Powell Basin and South Scotia Sea, ice-sheet-derived
623 meltwater may have acted as a driving mechanism fostering local sea-ice formation during winter, which
624 is not captured by the simulation in Holloway et al. (2017). Interestingly, the herein simulated sea ice at
625 the 128 ka BP time-slice corroborates our proxy-based data, indicating the presence of WSI in the
626 region amidst lower sea-ice concentration and continued retreat of sea ice over the spring/summer
627 seasons (Fig. 5.2). A similar sea-ice scenario is also established for the 125 ka BP time-slice,
628 considered to be the warmest period of the LIG (Fig. 5.3; Goelzer et al., 2016; Hoffman et al., 2017),
629 where Southern Hemisphere (SH) mid- to high-latitude spring insolation forcing reached a maximum
630 within the period from 130 ka BP to 125 ka BP (Lunt et al., 2013). The contrasting observation between
631 our marine sediment proxy and model data against that of the ice core $\delta^{18}\text{O}$ -accorded simulated-finding
632 emphasizes the need for more robust marine-based reconstructions, especially south of the modern
633 sea-ice edge, to sufficiently substantiate model results for these regions, and to enable comprehensive
634 input knowledge for future model simulations and predictions (Holloway et al., 2017; Otto-Bliesner et
635 al., 2013).

636 The reconstructed SSST trends in the Powell Basin and the South Scotia Sea are largely
637 comparable with the atmospheric temperature profile from the EDML ice core (Fig. 4h-j), suggesting
638 atmosphere-ocean interactions in the study area. The lack of significant glacial-interglacial temperature
639 variability within the Powell Basin could potentially be linked to its locality and close proximity to the
640 continental margin, where constant mixing of cold ice-shelf water with the WDW persists. Within the
641 Powell Basin, both the SSST and subsurface ocean temperature started to decrease around 130 ka
642 BP. While the SSST appeared to have cooled from -0.2°C to -0.4°C (127 ka BP) and recovered
643 thereafter – similar to the dip observed in the EDML $\delta^{18}\text{O}$ profile – the subsurface ocean temperature
644 declined distinctly from 0 to ca. -1.9°C and remained cold until 124 ka BP (Fig. 4g and h). The variance
645 in the magnitude of decline observed between the two temperature records (SSST vs. OT) may be
646 attributed to the distinctly different seasonal signals depicted by the proxies (i.e., summer vs. annual
647 temperature) and water depths (0-10 m vs. 0-200 m; see also Sect 4.2 and 4.3). We speculate that the
648 decline in seawater temperature since 130 ka BP may be the result of intense melting of the Antarctic
649 ice sheet and sea ice, leading to a freshening of coastal waters. Similar to the modern-day Weddell

650 Gyre circulation (see Sect 2 for details), the increased discharge of cold (sea) ice-shelf meltwater into
651 the Powell Basin, via the Antarctic Coastal Current and Antarctic Slope Current, may have deepened
652 the cold-water stratification in the basin, thus causing the observed dip in ocean temperature between
653 130 and 124 ka BP. Turney et al. (2020) discovered that the WAIS had retreated from the Patriot Hills
654 blue ice area by the end of TII (130.1 ± 1.8 ka BP). This area is located 50 km inland from the present-
655 day grounding line of the Filchner-Ronne Ice Shelf. Their investigation revealed a 50 kyrs hiatus in the
656 blue ice record, indicative of a collapse of the ice shelf at the end of TII, followed by its subsequent
657 recovery during late MIS 5. Holloway et al. (2016) also propose a maximum ice-sheet retreat at around
658 126 ka BP based on distinct differences between the isotopic records observed for Mt Moulton and East
659 Antarctic ice cores. Assuming that the distinct reduction in spring/summer sea-ice recorded in core
660 PS118_63-1 was not confined to the Powell Basin but may reflect a more extensive sea ice decline in
661 the Weddell Sea embayment, we posit that this loss of sea ice (i.e., the loss of an effective buffer
662 protecting ice-shelf fronts) may have accelerated the disintegration of the Weddell Sea ice shelves and,
663 ultimately, the WAIS.

664 Following the peak of the LIG around 119 ka BP, the Powell Basin sea-ice records reflect a cycle
665 of sea ice advance and retreat throughout the remaining MIS 5 substages. WSIC strengthened and
666 remained at ca. 80%, while spring/summer sea ice (PIPSO₂₅) experienced a substantial increase
667 between MIS 5e and 5d (reaching PGM values at 5d), and remained elevated (> ca. 0.6) for the rest of
668 the MIS (Fig. 4b and c). This expansion of sea ice into MIS 5d, and its persisting presence throughout
669 the remaining MIS 5, is accompanied by a gradual decline in both sea surface and subsurface ocean
670 temperatures, along with reduced primary production. Likewise, an increasing WSIC, lowered SSST
671 and primary productivity are also noted in the South Scotia Sea (Fig. 4d-h). However, being more
672 northerly located, the South Scotia Sea experienced a lower and more varied WSIC (ca. 48 - 68%)
673 and minimum summer sea-ice cover evident by a lower abundance of *F. obliquecostata* (<1%) than in
674 the Powell Basin (Fig. 4d).

675 5.1.3 Glacial period – Last Glacial Maximum – Termination I

676 After MIS 5, Antarctica transited into the last glacial period (74-19 ka BP). In our Powell Basin
677 records, this is reflected in a northward expansion of the sea-ice extent (peak PIPSO₂₅ values and 100%
678 WSIC). Additionally, the lack of sea ice- and phytoplankton-related biomarkers and diatoms points
679 towards an extremely suppressed production in the basin (Fig. 3a and b, 4b and c). We postulate that
680 at that time the basin was likely covered by permanent sea-ice cover or a floating ice shelf, which
681 inhibited primary production in the underlying water column. The South Scotia Sea record (PS67/219-
682 1) further to the north also points to an overall higher winter and summer sea-ice cover, with elevated
683 abundance of *F. obliquecostata* (0 - 3%) during this period suggesting a permanent sea-ice edge close
684 to the core site (Xiao et al., 2016a). The oscillating patterns observed in both the sea-ice record and the
685 biogenic opal content further point to alternating advance and retreat phases of the sea-ice edge in the
686 South Scotia Sea (Fig. 4d and f; Allen et al., 2011).

687 In the Powell Basin, capped by an overlying (sea) ice cover throughout the glacial period,
688 subsurface ocean temperatures somewhat resemble the millennial-scale variability in the EDML

689 temperature profile (Fig. 4g). We presume that the subsurface temperature variations may possibly
690 reflect changes in the ocean circulation in the Atlantic sector of the SO (Böhm et al., 2015; Williams et
691 al., 2021). However, the age uncertainties and the low resolution of our subsurface ocean temperature
692 record hamper an affirmative conclusion, and more data points will be required to ascertain
693 corresponding oceanic variability.

694 The last glacial period culminated during the LGM between 26.5 and 19 ka BP with a most
695 northwardly extending sea-ice edge, as identified in several marine sediment cores (Fig. 4b and c;
696 Gersonde et al., 2005; Xiao et al., 2016a) and deduced from maximum ssNa⁺ concentrations in the
697 EDML ice core (Fig. 4a; Fischer et al., 2007). Evidence from previous studies indicated the advance of
698 grounded ice sheet and island ice caps to the edge of the outer continental shelf (Davies et al., 2012;
699 Dickens et al., 2014). These grounded ice sheets were surrounded by floating ice shelves that extended
700 seaward to 58°S on the western side of Antarctica (Herron and Anderson, 1990; Johnson and Andrews,
701 1986). In the Atlantic sector, the 60 - 70% expansion of WSI towards the modern Polar Front (~50°S;
702 Gersonde et al., 2003) also promoted a northward shift of the summer sea-ice edge beyond core site
703 PS67/219-1 to around 55°S (Allen et al., 2011; Collins et al., 2012), which lead to restricted primary
704 productivity as reflected in the minimum biogenic opal content of core PS67/219-1 (Fig. 4f). The LGM
705 is also considered the coldest interval, with a northward expansion of the (sub)Antarctic cold waters by
706 4 - 5° in latitude towards the subtropical warm waters (Gersonde and Zielinski, 2000; Gersonde et al.,
707 2003). Sea-ice extent (Fig. 5.4) and SSST (Fig. 6.3) derived from our climate simulation during the peak
708 of LGM (21 ka BP) align with these findings. This distinct growth of the (sea) ice-field in the SO, coupled
709 with lower reconstructed and modeled LGM subsurface temperatures (Fig. 4g and 7.3), suggests an
710 intensified cold-water stratification at our core sites, and a possible northward displacement of the WDW
711 upwelling zone towards the edge of the summer sea-ice field (Ferrari et al., 2014).

712 TI began around 18 ka BP, when our records from Powell Basin indicate a transition from a
713 perennial-ice cover to a dynamic sea-ice scenario (see Sect 4.5), with several cycles of advance and
714 retreat. Similarly, the sea ice-related records from the South Scotia Sea (PS67/219-1) and the EDML
715 ssNa⁺ record depict a decrease in sea-ice cover, along with rapid increases in primary productivity and
716 ocean temperature (Fig. 4). This deglaciation is attributed to a weakening AMOC circulation as a result
717 of reduced NADW formation caused by increasing NH summer insolation and significant ice sheet melt
718 at 18 ka BP, also known as Heinrich Stadial 1 (Clark et al., 2020; Denton et al., 2010; Waelbroeck et
719 al., 2011). The gradual warming of TI was interrupted by a brief cooling between 14 and 12 ka BP.
720 During this interval, our records reveal a short-term re-advancement in sea ice, coupled with a drop in
721 productivity and temperature (Fig. 4). This event seems to coincide with multiple South Atlantic records
722 (Xiao et al., 2016a) and higher ssNa⁺ concentrations and a plateau in $\delta^{18}\text{O}$ values recorded in the EDML
723 ice core (Fischer et al., 2007). We hence propose this event to be the Antarctic Cold Reversal (ACR),
724 which is linked to the Bølling-Allerød warm interval in the NH via the bipolar seesaw mechanism (Pedro
725 et al., 2011; 2016).

726 5.1.4 Holocene

727 Following the brief cooling of the ACR, the deglacial warming resumed its pace and Antarctica
728 transited into the present interglacial (Holocene: 12 ka BP-present), which is marked by intervals of
729 warming and cooling events (Bentley et al., 2009; Bianchi and Gersonde, 2004; Xiao et al., 2016a). Our
730 data support these findings and document periods characterized by seasonal/dynamic and minimum
731 sea-ice cover (see Sect 4.5) since 12 ka BP. We acknowledge that the age constraints and data
732 availability of core PS118_63-1 for the Holocene is limited and exercise caution on the interpretation of
733 the Holocene proxy records. Nevertheless, our data still permit the discrimination of Holocene warming
734 and cooling trends.

735 The Powell Basin experienced an overall rapid decline in the winter and spring/summer sea-ice
736 (Fig. 4b and c), concurrent with a rise in SSST (-0.5 to 0.5°C; Fig. 4h) and primary productivity between
737 12 and 5 ka PB (Fig. 4e), suggesting a seasonal sea-ice cover. The significant reduction in the
738 abundance of the *F. curta* gp (below 3%), WSIC and spring/summer sea ice (PIPSO₂₅; Fig. 4b and c)
739 culminates at ca. 5 ka BP and is accompanied by an elevated primary productivity reflected in rising
740 biogenic opal and TOC contents, which seems to indicate a brief open-ocean setting for the Powell
741 Basin during this warm interval. We further note fluctuating SSSTs, while the subsurface ocean
742 temperature remains relatively stable between 9 and 5 ka BP and the remainder of the Holocene (Fig.
743 4g and h). This somehow contrasts with a subtle decline in SSSTs recorded in core PS67/219-1 (Fig.
744 4i) in the South Scotia Sea, substantiated by the elevated presence of *Chaetoceros* rs recorded in core
745 PS118_63-1 (Fig. 3e). We may attribute this cooling to a northward export of increased glacial
746 meltwater. Our model simulation at 6 ka BP depicts a somewhat similar oceanic condition, with <40%
747 spring/summer sea ice at the studied sites (Fig. 5.5a). However, in comparison with our proxy records,
748 the model appears to have overestimated the WSI, SST and OT (Fig. 5.5b, 6.4 and 7.4). This
749 overestimation may be attributed to the complex ice-ocean interactions and feedbacks along the
750 Antarctic coastal region, which may not be fully represented in the model that has a spatial resolution
751 in the order of tens of kilometers and does not reflect any ice sheet dynamics.

752 While the limited age constraints for the Holocene in core PS118_63-1, preclude us from further
753 allocating short-term climate variations, we propose that the interval around 5 ka BP may reflect the
754 Holocene climate optimum, while the upper part of the core depicts the later Holocene conditions. Here,
755 increasing PIPSO₂₅ values and WSI reflect a re-expansion of seasonal sea ice still permitting primary
756 productivity as derived from elevated biogenic opal and TOC contents (Fig. 4b, c and e). The climate
757 optimum experienced in the Powell Basin seems to correspond to the mid-Holocene climate optimum
758 identified in sediment cores from the South Orkney Plateau between 8.2 and 4.8 ka BP and around
759 Antarctica (Crosta et al., 2008; Denis et al., 2010; Kim et al., 2012; Lee et al., 2010; Taylor et al., 2001).
760 However, reports of differing timings and mode for the mid-Holocene climate optimum around the
761 Antarctic Peninsula have been noted in previous studies (Bentley et al., 2009; Davies et al., 2012;
762 Shevenell et al., 1996; Taylor and Sjunneskog, 2002). Vorrath et al. (2023) determined the mid-
763 Holocene climate optimum to have occurred between 8.2 and 4.2 ka BP, based on biomarker analyses
764 of a sediment core from the eastern Bransfield Strait. They suggest that the climatic changes at their
765 core site were influenced predominantly by the warm Antarctic Circumpolar Current rather than the

766 cold-water Weddell Sea. This is contrary to a shorter climate optimum (6.8-5.9 ka BP) proposed by
767 Heroy et al. (2008), where they examined the climate history of western Bransfield Strait using sediment
768 and diatom analyses. Such diverse research outcomes highlight the complexity of responses to micro-
769 region variations in glacial, atmospheric and oceanic changes in the Antarctic Peninsula throughout the
770 Holocene (Bentley et al., 2009; Davies et al., 2012; Heroy et al., 2008; Vorrath et al., 2023).

771 **5.2 Comparison between interglacials / transition periods**

772 A comparison of the environmental changes caused by climate warming during TII and TI as well
773 as the peak LIG and the Holocene, may yield valuable information on common or different driving and
774 feedback mechanisms. As marine cores PS118_63-1 and PS67/219-1 provide continuous records of
775 the environmental evolution in the northwestern Weddell Sea and South Scotia Sea, respectively, dating
776 back to at least 145 ka BP, they offer a distinct opportunity to evaluate (sea-ice) conditions between the
777 two terminations (TII and TI) and both warm periods (LIG and Holocene), particularly in proximity to the
778 continental margin. Denton et al. (2010) studied the last four terminations and concluded that the
779 terminations were triggered by a sequence of comparable events: maximum NH summer insolation that
780 caused substantial NH ice sheet melting (due to marine ice sheet instability) over an extended (>5 kyrs)
781 NH stadial interval. The huge release of meltwater slowed the AMOC, thus triggering an intense
782 warming in the southern high-latitudes through the bipolar seesaw teleconnection, accompanied by a
783 poleward shift in the southern westerlies. In line with this hypothesis, our records from cores PS118_63-
784 1 and PS67/219-1 portray a consistent and rapid decline in sea ice throughout both terminations (TII
785 and TI). Interestingly, both deglaciations feature a short-term readvance of sea ice during their latest
786 stage, at ca. 130 ka BP and during the ACR, respectively, likely due to meltwater-discharge from
787 retreating ice shelves/ice sheets in the SO. This suggests that short-term sea ice growth stimulated by
788 deglacial meltwater may be a common feature during glacial terminations. Despite commonalities in the
789 sea-ice records, some differences are discernible. For instance, during TII, there is an abrupt surge in
790 biogenic opal in the South Scotia Sea, along a consistent rise in TOC content within the Powell Basin.
791 In contrast, TI exhibits a pattern characterized by a gradual increase with periodic fluctuations
792 throughout the termination for both TOC and biogenic opal content. Additionally, the South Scotia Sea
793 (PS67/219-1) recorded a higher mean biogenic opal content and SSST across TII (35%; 0.7°C) than TI
794 (26%; 0.5°C). Likewise, in the Powell Basin (PS118_63-1), higher mean TOC and subsurface ocean
795 temperature are perceived during TII (0.5%; 0°C) than during TI (0.4%; -0.3°C). These data are in
796 agreement with the EDML $\delta^{18}\text{O}$ record, which registered a stronger deglacial amplitude (32%) in TII
797 than TI (Masson-Delmotte et al., 2011). Broecker and Henderson (1998) also speculated that the
798 amplitude of the SH summer insolation during TII was higher than during TI. Additionally, a delay of
799 approximately 10 kyrs between the SH and NH summer insolation (and subsequent NH ice sheet
800 melting) during TII – as compared to TI's SH summer insolation peak just before the melting of the NH
801 ice sheet – probably contributed to a more pronounced TII warming in the SO. The differing magnitude
802 of warming observed between both core sites in the South Atlantic, however, is likely attributed to their
803 latitudinal differences.

804 The climate during the LIG appeared to be warmer than during the Holocene. In the Powell Basin,
805 the LIG peak interval (i.e., MIS 5e) was characterized by a significantly reduced spring/summer sea-ice
806 cover and peak productivity, while a higher spring/summer sea-ice cover, along with an only gradually
807 increasing productivity are observed for the Holocene warm period (Fig. 4b and e). However, no
808 significant difference in the WSIC between both interglacial was noted. The discrepancy in warming
809 intensity likely occurred seasonally and coincided with maximum summer insolation (see also Fig. 4 in
810 Bova et al., 2021). Nonetheless, a lower mean annual regional insolation (-1.1 W/m² difference; Laskar
811 et al., 2004) during the LIG does not explain the warmer conditions observed in the region. Bova et al.
812 (2021) hypothesized that the LIG was relatively warmer than the Holocene as a result of its preceding
813 deglacial dynamics: specifically, the magnitude of the last deglaciation was half that of the penultimate
814 deglaciation – where a rapid and intense warming destabilized and significantly reduced the (sea) ice
815 cover to near modern-day level by the onset of the LIG (Bova et al., 2021), and possibly a collapse of
816 the WAIS in the first half of the LIG (Pollard and Deconto, 2009; Sutter et al., 2016). As such, we opine
817 that the lower magnitude of warming during TI was a consequence of spatially and temporally varying
818 retreats and advances in ice cover (including sea ice, ice shelves and glaciers) in the SO. The higher
819 ice coverage throughout the Holocene resulted in a higher surface albedo and a cooler Holocene, as
820 compared to the LIG. This is witnessed in our rather variable Holocene sea-ice proxy records (Fig. 4b
821 and c) and differing reports of mid-Holocene warming and repeated fluctuations in environmental
822 conditions around Antarctica (see sect 5.1.4; Bentley et al., 2014; Davies et al., 2012; Ó Cofaigh et al.,
823 2014).

824 **5.3 Evaluating COSMOS performance: Addressing boundary conditions and model selection**

825 With regard to COSMOS simulations, we note very similar sea-ice conditions being depicted for
826 the peak interglacial 125 ka BP and 6 ka BP time slices (Fig 5.3 and 5.5), while subtle differences are
827 resolved for SSTs and OTs (Fig. 6.2 and 6.4, 7.2 and 7.4, respectively). When considering the disparity
828 observed in our proxy data between these two interglacial intervals, we infer that these similarities in
829 the simulations likely result from using the same geographic boundary conditions for both time slices,
830 while climate forcing data (e.g., greenhouse gases, orbital parameters) differ, of course. Our study
831 aligns with the PMIP framework in maintaining a constant modern-day geography across each
832 interglacial time slice, specifically the mid-Holocene (e.g., 6 ka BP) and the LIG (e.g., 128 and 125 ka
833 BP). For the 6 ka BP time slice, this decision is supported by evidence indicating that ice sheets had
834 reached their modern configuration (Otto-Bliesner et al., 2017). In the case of the LIG, the use of the
835 modern ice-sheet configuration is primarily due to uncertainties in the LIG reconstructions (Otto-Bliesner
836 et al., 2017). We acknowledge that the consideration of a single geographic configuration throughout
837 the LIG certainly is a simplification. However, it is also important to note that the changes in the Antarctic
838 ice sheets' contribution to global mean sea level were small between 128 and 125 ka BP, compared to
839 the remainder of the LIG (Barnett et al., 2023). Therefore, we propose that using a constant ice-sheet
840 configuration for our LIG time slices is a reasonable approximation – in particular when we consider the
841 lack of robust alternative ice sheet configurations that could have been used as a boundary condition
842 for the climate model. Similarly, we estimated a constant ice-sheet setting for both the PGM and LGM

843 time slices. While there are indications of different NH ice- sheet extents between the two glacial periods
844 (Rohling et al., 2017), uncertainty remains regarding the exact distribution of ice on Antarctica.
845 Understanding this distribution is crucial to determine whether different ice-sheet configurations should
846 be considered for the boundary conditions of the respective glacial climate simulations. Given the varied
847 trends observed in our proxy data for each glacial and interglacial periods, we propose that future
848 studies should explore different plausible Antarctic ice-sheet configurations and their effects on glacial-
849 interglacial sea ice and oceanic conditions in the SO, particularly in the coastal regions.

850 In our modeling approach, we have relied exclusively on simulations from COSMOS rather than
851 adopting a multi-model approach based on available PMIP simulations. This decision was motivated by
852 the need to cover specific time slices pertinent to our study (see also Sect 3.5). To validate the reliability
853 of our results, we conducted a comparison of COSMOS-simulated sea-ice cover and SST results
854 against those from the PMIP3 and PMIP4 ensemble models. We refer to Supplement S3.4 for full detail.
855 In general, the model-to-model comparison shows good agreement ($<2\sigma$ threshold) between our
856 COSMOS results and those from the PMIP3 ensemble – especially at our study locations, with some
857 disagreement noted for the 21 ka BP time slice (Supplementary Fig. S4 and S5, S8 and S9). These
858 deviations largely occur around the sea-ice edge and are primarily due to uncertainties generated within
859 the PMIP3 ensemble itself. In contrast, our COSMOS-to-PMIP4 ensemble comparison shows greater
860 disagreement. The COSMOS simulation shows a milder warm bias in the SO compared to various other
861 PMIP3 models (Lunt et al., 2013), whereas CMIP6 models, which provide the foundation for PMIP4,
862 are documented to have a warm bias in the SO (Luo et al., 2023). Beyond the difference in warm bias,
863 the disagreements between COSMOS and PMIP4 may arise from several factors, including evolution
864 of modeling protocols, boundary conditions, and model development from PMIP3 to PMIP4, with
865 COSMOS remaining a PMIP3-class model. Based on the comparative outcomes, we demonstrate that
866 our results align with PMIP in many relevant aspects, though this comparison is limited by the
867 incomplete coverage of time slices within PMIP. Where our model shows disagreement with the PMIP3
868 ensemble, the uncertainty within the ensemble itself is quite large. This highlights that the uncertainty
869 in simulated sea-ice conditions at our core locations, which we acknowledge as a limitation of using
870 only one model in our study, is not necessarily mitigated by using an ensemble of models instead. Given
871 that COSMOS is mostly within the 2σ threshold – defined as a measure for agreement with the PMIP3
872 ensemble – at the study sites, we would not expect to derive substantially different inferences if we
873 relied on the PMIP3 ensemble instead. Although COSMOS has not undergone the updates that PMIP4
874 models received and has been exposed to boundary conditions only partly comparable to PMIP4
875 simulations, to date it remains one of the most extensively utilized models for reconstructing Quaternary
876 climates and beyond. This enables our study's results to be considered within the much larger context
877 of the Cenozoic climate. Despite the aforementioned limitations, it is worth noting that COSMOS has
878 been successfully employed alongside other PMIP4 models (Stepanek et al., 2020).

879 **6 Summary and conclusions**

880 Multiproxy analyses on marine sediment core PS118_63-1 from the Powell Basin provide new
881 insights into the glacial-interglacial environmental variability in proximity to the Antarctic continental
882 margin. With the use of the novel sea ice and open-water biomarkers and diatom assemblage data,
883 alongside primary productivity proxies, we are able to reconstruct sea-ice conditions in the Powell Basin
884 for the past ca. 145 kyrs. Our findings reveal year-round ice-cover with minimal productivity during
885 glacial periods, while dynamic sea-ice conditions with varied productivity are recorded in the Powell
886 Basin during climate transitions and interglacial periods, such as the Holocene and MIS 5. Peak
887 reduction in sea ice and near open ocean conditions are noted for MIS 5e. In contrast, no significant
888 glacial-interglacial temperature variation was registered in the basin, which is attributed to the cold-
889 water regime of the Weddell Sea. Comparison between the current and last interglacial, and their
890 respective climate transitions (TI and TII), suggests a relationship between deglacial amplitude and
891 warming intensity during the corresponding interglacial: in general, an abrupt and intense (gradual and
892 slow) deglaciation leads to a warmer (cooler) interglacial, with higher (lesser) ice-sheet retreat (Bova et
893 al., 2021). Our data presented in this study reinforce earlier paleo sea-ice reconstructions in the South
894 Atlantic sector of the SO and provide new insights into the ice-proximal sea-ice response during varying
895 climate conditions. Evaluation of both proxy and model data highlights similarities between sea-ice
896 reconstruction and simulation. However, notable discrepancies remain, such as the differing proxy-
897 model data observed for the Holocene compared to the LIG, and subsurface temperature profile for the
898 LIG. It is therefore pivotal to explore different Antarctic ice-sheet configurations in future studies, as well
899 to expand on the paleoclimate data for the region. These will help to close the gap in our understanding
900 of ocean-ice-atmosphere interactions and dynamics and ultimately enhance climate model predictions
901 closer to the Antarctic continental margins.

902

903 **Data availability.** Proxy data mentioned in this article will be available at
904 <https://doi.org/10.1594/PANGAEA.965042> (Khoo et al., 2024), and COSMOS model output will be
905 accessible at <https://doi.org/10.1594/PANGAEA.972654> (Stepanek et al., 2024). For specific model
906 output requests beyond the climate variables included in the PANGAEA data publication, please contact
907 Christian Stepanek at christian.stepanek@awi.de. CMIP/PMIP data is available via the Earth System
908 Grid Federation using one of their publicly available data portals (e.g., [https://esgf-
909 data.dkrz.de/search/cmip5-dkrz/](https://esgf-data.dkrz.de/search/cmip5-dkrz/) and <https://esgf-data.dkrz.de/search/cmip6-dkrz/>).

910

911 **Code availability.** Requests for the source code of the COSMOS climate model should be directed to
912 the Max Planck Institute for Meteorology, Bundesstrasse 53, 20146 Hamburg, Germany.

913

914 **Supplement.** The supplement related to this article is available online at:

915

916 **Author contributions.** This study was conceived by WWK and JM. Data collection and interpretation
917 was conducted by WWK, together with OE (diatom), JM (HBI), JH and GM (GDGT). WG produced the
918 U/Th-dating data. CS and GL selected, documented, and post-processed the data from an ensemble

919 of simulations that provided the climate model data for this study. Three of the six simulations presented
920 here, namely *lig125k*, *lig128k*, and *pgm140k*, represent previously unpublished climate model output
921 created by PG. WX supplied unpublished data for PS67/219-1. WWK wrote the paper and created the
922 visualizations, supported by CS who visualized model output and interpolated climate model output to
923 core locations. JM supervised the study. All authors contributed to the analyses, discussion of the
924 results, and the conclusion of this study.

925

926 **Competing interests.** The authors declare that they have no conflict of interest.

927

928 **Acknowledgements.** We thank the captain, crew and science team of the RV Polarstern cruise PS118
929 (Grant No. AWI_PS118_04). Special thanks go to Michael Schreck, Nele Steinberg, Sabine Hanisch
930 and Frank Niessen for PS118 marine geology operations. Appreciation is also extended to Denise
931 Diekstatt (HBI), Mandy Kuck (HBI), Ulrike Böttjer (Biogenic Opal) for their support. Simon Belt is
932 acknowledged for providing the 7-HND internal standard for HBI quantification. This research is funded
933 through the Alfred Wegener Institute Helmholtz Centre for Polar and Marine Research (International
934 Science Program for Integrative Research in Earth Systems, INSPIRES II). Gerrit Lohmann, Paul Gierz,
935 and Christian Stepanek are funded through the Alfred Wegener Institute's research program: Changing
936 Earth - Sustaining our Future of the Helmholtz Association. Christian Stepanek also acknowledges
937 funding from the Helmholtz Climate Initiative REKLIM. We acknowledge the World Climate Research
938 Programme's Working Group on Coupled Modeling for CMIP, and the Paleoclimate Model
939 Intercomparison Project and its working groups for coordinating the model intercomparison in PMIP3
940 and PMIP4. Appreciation is extended to the climate modeling groups (listed in Table S4) for their
941 contribution and availability of model output to CMIP5/6 and PMIP3/4. The U.S. Department of Energy's
942 Program for Climate Model Diagnosis and Intercomparison is recognized for providing coordinating
943 support and leading software infrastructure development with the Global Organization for Earth System
944 Science Portals. The Earth System Grid Federation is also acknowledged for preserving and providing
945 CMIP and PMIP model output. We are also appreciative of the support from the Alfred Wegener
946 Institute's Open Access Publication Funds. Lastly, we thank the editor, Dr. Alberto Reyes, Dr. Xavier
947 Crosta and an anonymous reviewer for their constructive comments that helped to improve the paper.

948 **References**

949 Abe-Ouchi, A., Saito, F., Kageyama, M., Braconnot, P., Harrison, S. P., Lambeck, K., Otto-Bliesner, B.
950 L., Peltier, W. R., Tarasov, L., Peterschmitt, J. Y., and Takahashi, K.: Ice-sheet configuration in the
951 CMIP5/PMIP3 Last Glacial Maximum experiments, *Geosci. Model Dev.*, 8, 3621-3637,
952 <https://doi.org/10.5194/gmd-8-3621-2015>, 2015.

953 Abernathy, R. P., Cerovecki, I., Holland, P. R., Newsom, E., Mazloff, M., and Talley, L. D.: Water-mass
954 transformation by sea ice in the upper branch of the Southern Ocean overturning, *Nature Geoscience*,
955 9, 596-601, <https://doi.org/10.1038/ngeo2749>, 2016.

956 Abram, N. J., Wolff, E. W., and Curran, M. A. J.: A review of sea ice proxy information from polar ice
957 cores, *Quaternary Science Reviews*, 79, 168-183, <https://doi.org/10.1016/j.quascirev.2013.01.011>,
958 2013.

- 959 Allen, C. S., Pike, J., and Pudsey, C. J.: Last glacial–interglacial sea-ice cover in the SW Atlantic and
 960 its potential role in global deglaciation, *Quaternary Science Reviews*, 30, 2446-2458,
 961 <https://doi.org/10.1016/j.quascirev.2011.04.002>, 2011.
- 962 Argus, D. F. and Peltier, W. R.: Constraining models of postglacial rebound using space geodesy: a
 963 detailed assessment of model ICE-5G (VM2) and its relatives, *Geophysical Journal International*, 181,
 964 697-723, <https://doi.org/10.1111/j.1365-246X.2010.04562.x>, 2010.
- 965 Bakker, P., Masson-Delmotte, V., Martrat, B., Charbit, S., Renssen, H., Gröger, M., Krebs-Kanzow, U.,
 966 Lohmann, G., Lunt, D. J., Pfeiffer, M., Phipps, S. J., Prange, M., Ritz, S. P., Schulz, M., Stenni, B.,
 967 Stone, E. J., and Varma, V.: Temperature trends during the Present and Last Interglacial periods – a
 968 multi-model-data comparison, *Quaternary Science Reviews*, 99, 224-243,
 969 <https://doi.org/10.1016/j.quascirev.2014.06.031>, 2014.
- 970 Barbara, L., Crosta, X., Schmidt, S., and Massé, G.: Diatoms and biomarkers evidence for major
 971 changes in sea ice conditions prior the instrumental period in Antarctic Peninsula, *Quaternary Science*
 972 *Reviews*, 79, 99-110, <https://doi.org/10.1016/j.quascirev.2013.07.021>, 2013.
- 973 Barbara, L., Crosta, X., Leventer, A., Schmidt, S., Etourneau, J., Domack, E., and Massé, G.:
 974 Environmental responses of the Northeast Antarctic Peninsula to the Holocene climate variability,
 975 *Paleoceanography*, 31, 131-147, <https://doi.org/10.1002/2015PA002785>, 2016.
- 976 Barnett, R. L., Austermann, J., Dyer, B., Telfer, M. W., Barlow, N. L. M., Boulton, S. J., Carr, A. S., and
 977 Creel, R. C.: Constraining the contribution of the Antarctic Ice Sheet to Last Interglacial sea level,
 978 *Science Advances*, 9, eadf0198, <https://doi.org/10.1126/sciadv.adf0198>, 2023.
- 979 Belt, S. T.: Source-specific biomarkers as proxies for Arctic and Antarctic sea ice, *Organic*
 980 *Geochemistry*, 125, 277-298, <https://doi.org/10.1016/j.orggeochem.2018.10.002>, 2018.
- 981 Belt, S. T. and Müller, J.: The Arctic sea ice biomarker IP25: a review of current understanding,
 982 recommendations for future research and applications in palaeo sea ice reconstructions, *Quaternary*
 983 *Science Reviews*, 79, 9-25, <https://doi.org/10.1016/j.quascirev.2012.12.001>, 2013.
- 984 Belt, S. T., Allard, W. G., Massé, G., Robert, J.-M., and Rowland, S. J.: Highly branched isoprenoids
 985 (HBIs): identification of the most common and abundant sedimentary isomers, *Geochimica et*
 986 *Cosmochimica Acta*, 64, 3839-3851, [https://doi.org/10.1016/S0016-7037\(00\)00464-6](https://doi.org/10.1016/S0016-7037(00)00464-6), 2000.
- 987 Belt, S. T., Brown, T. A., Rodriguez, A. N., Sanz, P. C., Tonkin, A., and Ingle, R.: A reproducible method
 988 for the extraction, identification and quantification of the Arctic sea ice proxy IP25 from marine
 989 sediments, *Analytical Methods*, 4, 705-713, <https://doi.org/10.1039/C2AY05728J>, 2012.
- 990 Belt, S. T., Smik, L., Brown, T. A., Kim, J. H., Rowland, S. J., Allen, C. S., Gal, J. K., Shin, K. H., Lee,
 991 J. I., and Taylor, K. W. R.: Source identification and distribution reveals the potential of the geochemical
 992 Antarctic sea ice proxy IPSO25, *Nature Communications*, 7, 12655,
 993 <https://doi.org/10.1038/ncomms12655>, 2016.
- 994 Bentley, M. J., Hodgson, D. A., Smith, J. A., Cofaigh, C. Ó., Domack, E. W., Larter, R. D., Roberts, S.
 995 J., Brachfeld, S., Leventer, A., Hjort, C., Hillenbrand, C.-D., and Evans, J.: Mechanisms of Holocene
 996 palaeoenvironmental change in the Antarctic Peninsula region, *The Holocene*, 19, 51-69,
 997 <https://doi.org/10.1177/0959683608096603>, 2009.
- 998 Bentley, M. J., Ó Cofaigh, C., Anderson, J. B., Conway, H., Davies, B., Graham, A. G. C., Hillenbrand,
 999 C.-D., Hodgson, D. A., Jamieson, S. S. R., Larter, R. D., Mackintosh, A., Smith, J. A., Verleyen, E.,
 1000 Ackert, R. P., Bart, P. J., Berg, S., Brunstein, D., Canals, M., Colhoun, E. A., Crosta, X., Dickens, W.
 1001 A., Domack, E., Dowdeswell, J. A., Dunbar, R., Ehrmann, W., Evans, J., Favier, V., Fink, D., Fogwill,
 1002 C. J., Glasser, N. F., Gohl, K., Golledge, N. R., Goodwin, I., Gore, D. B., Greenwood, S. L., Hall, B. L.,
 1003 Hall, K., Hedding, D. W., Hein, A. S., Hocking, E. P., Jakobsson, M., Johnson, J. S., Jomelli, V., Jones,
 1004 R. S., Klages, J. P., Kristoffersen, Y., Kuhn, G., Leventer, A., Licht, K., Lilly, K., Lindow, J., Livingstone,
 1005 S. J., Massé, G., McGlone, M. S., McKay, R. M., Melles, M., Miura, H., Mulvaney, R., Nel, W., Nitsche,
 1006 F. O., O'Brien, P. E., Post, A. L., Roberts, S. J., Saunders, K. M., Selkirk, P. M., Simms, A. R., Spiegel,

- 1007 C., Stollendorf, T. D., Sugden, D. E., van der Putten, N., van Ommen, T., Verfaillie, D., Vyverman, W.,
 1008 Wagner, B., White, D. A., Witus, A. E., and Zwartz, D.: A community-based geological reconstruction
 1009 of Antarctic Ice Sheet deglaciation since the Last Glacial Maximum, *Quaternary Science Reviews*, 100,
 1010 1-9, <https://doi.org/10.1016/j.quascirev.2014.06.025>, 2014.
- 1011 Bianchi, C. and Gersonde, R.: The Southern Ocean surface between Marine Isotope Stages 6 and 5d:
 1012 Shape and timing of climate changes, *Palaeogeography, Palaeoclimatology, Palaeoecology*, 187, 151-
 1013 177, [https://doi.org/10.1016/S0031-0182\(02\)00516-3](https://doi.org/10.1016/S0031-0182(02)00516-3), 2002.
- 1014 Bianchi, C. and Gersonde, R.: Climate evolution at the last deglaciation: the role of the Southern Ocean,
 1015 *Earth and Planetary Science Letters*, 228, 407-424, <https://doi.org/10.1016/j.epsl.2004.10.003>, 2004.
- 1016 Böhm, E., Lippold, J., Gutjahr, M., Frank, M., Blaser, P., Antz, B., Fohlmeister, J., Frank, N., Andersen,
 1017 M. B., and Deininger, M.: Strong and deep Atlantic meridional overturning circulation during the last
 1018 glacial cycle, *Nature*, 517, 73-76, <https://doi.org/10.1038/nature14059>, 2015.
- 1019 Bova, S., Rosenthal, Y., Liu, Z., Godad, S. P., and Yan, M.: Seasonal origin of the thermal maxima at
 1020 the Holocene and the last interglacial, *Nature*, 589, 548-553, <https://doi.org/10.1038/s41586-020-03155-x>, 2021.
- 1022 Braconnot, P., Harrison, S. P., Kageyama, M., Bartlein, P. J., Masson-Delmotte, V., Abe-Ouchi, A.,
 1023 Otto-Bliesner, B., and Zhao, Y.: Evaluation of climate models using palaeoclimatic data, *Nature Climate*
 1024 *Change*, 2, 417-424, <https://doi.org/10.1038/nclimate1456>, 2012.
- 1025 Broecker, W. S. and Henderson, G. M.: The sequence of events surrounding Termination II and their
 1026 implications for the cause of glacial-interglacial CO₂ changes, *Paleoceanography*, 13, 352-364,
 1027 <https://doi.org/10.1029/98PA00920>, 1998.
- 1028 Brovkin, V., Raddatz, T., Reick, C. H., Claussen, M., and Gayler, V.: Global biogeophysical interactions
 1029 between forest and climate, *Geophysical Research Letters*, 36, <https://doi.org/10.1029/2009GL037543>,
 1030 2009.
- 1031 Carmack, E. C. and Foster, T. D.: On the flow of water out of the Weddell Sea, *Deep Sea Research*
 1032 *and Oceanographic Abstracts*, 22, 711-724, [https://doi.org/10.1016/0011-7471\(75\)90077-7](https://doi.org/10.1016/0011-7471(75)90077-7), 1975.
- 1033 Chadwick, M., Allen, C. S., Sime, L. C., and Hillenbrand, C. D.: Analysing the timing of peak warming
 1034 and minimum winter sea-ice extent in the Southern Ocean during MIS 5e, *Quaternary Science Reviews*,
 1035 229, 106134, <https://doi.org/10.1016/j.quascirev.2019.106134>, 2020.
- 1036 Chadwick, M., Allen, C. S., Sime, L. C., Crosta, X., and Hillenbrand, C. D.: Reconstructing Antarctic
 1037 winter sea-ice extent during Marine Isotope Stage 5e, *Clim. Past*, 18, 129-146,
 1038 <https://doi.org/10.5194/cp-18-129-2022>, 2022.
- 1039 Chadwick, M., Jones, J., Lawler, K.-A., Prebble, J., Kohfeld, K. E., and Crosta, X.: Understanding
 1040 glacial-interglacial changes in Southern Ocean sea ice, *Past Global Changes Magazine*, 27(2), 86,
 1041 <https://doi.org/10.22498/pages.27.2.86>, 2019.
- 1042 Clark, P. U., He, F., Golledge, N. R., Mitrovica, J. X., Dutton, A., Hoffman, J. S., and Dendy, S.: Oceanic
 1043 forcing of penultimate deglacial and last interglacial sea-level rise, *Nature*, 577, 660-664,
 1044 <https://doi.org/10.1038/s41586-020-1931-7>, 2020.
- 1045 Collins, L. G., Pike, J., Allen, C. S., and Hodgson, D. A.: High-resolution reconstruction of southwest
 1046 Atlantic sea-ice and its role in the carbon cycle during marine isotope stages 3 and 2,
 1047 *Paleoceanography*, 27, <https://doi.org/10.1029/2011PA002264>, 2012.
- 1048 Collins, L. G., Allen, C. S., Pike, J., Hodgson, D. A., Weckström, K., and Massé, G.: Evaluating highly
 1049 branched isoprenoid (HBI) biomarkers as a novel Antarctic sea-ice proxy in deep ocean glacial age
 1050 sediments, *Quaternary Science Reviews*, 79, 87-98, <https://doi.org/10.1016/j.quascirev.2013.02.004>,
 1051 2013.

- 1052 Coren, F., Ceccone, G., Lodolo, E., Zanolla, C., Zitellini, N., Bonazzi, C., and Centonze, J.: Morphology,
1053 seismic structure and tectonic development of the Powell Basin, Antarctica, *Journal of the Geological*
1054 *Society*, 154, 849-862, <https://doi.org/10.1144/gsjgs.154.5.0849>, 1997.
- 1055 Cortese, G. and Abelmann, A.: Radiolarian-based paleotemperatures during the last 160 kyr at ODP
1056 Site 1089 (Southern Ocean, Atlantic Sector), *Palaeogeography, Palaeoclimatology, Palaeoecology*,
1057 182, 259-286, [https://doi.org/10.1016/S0031-0182\(01\)00499-0](https://doi.org/10.1016/S0031-0182(01)00499-0), 2002.
- 1058 Crosta, X., Denis, D., and Ther, O.: Sea ice seasonality during the Holocene, Adélie Land, East
1059 Antarctica, *Marine Micropaleontology*, 66, 222-232, <https://doi.org/10.1016/j.marmicro.2007.10.001>,
1060 2008.
- 1061 Crosta, X., Pichon, J.-J., and Labracherie, M.: Distribution of Chaetoceros resting spores in modern
1062 peri-Antarctic sediments, *Marine Micropaleontology*, 29, 283-299, [https://doi.org/10.1016/S0377-
1063 8398\(96\)00033-3](https://doi.org/10.1016/S0377-8398(96)00033-3), 1997.
- 1064 Crosta, X., Kohfeld, K. E., Bostock, H. C., Chadwick, M., Du Vivier, A., Esper, O., Etourneau, J., Jones,
1065 J., Leventer, A., Müller, J., Rhodes, R. H., Allen, C. S., Ghadi, P., Lamping, N., Lange, C. B., Lawler, K.
1066 A., Lund, D., Marzocchi, A., Meissner, K. J., Menviel, L., Nair, A., Patterson, M., Pike, J., Prebble, J. G.,
1067 Riesselman, C., Sadatzki, H., Sime, L. C., Shukla, S. K., Thöle, L., Vorrath, M. E., Xiao, W., and Yang,
1068 J.: Antarctic sea ice over the past 130,000 years – Part 1: a review of what proxy records tell us, *Clim.*
1069 *Past*, 18, 1729-1756, <https://doi.org/10.5194/cp-18-1729-2022>, 2022.
- 1070 Dallmeyer, A., Claussen, M., Wang, Y., and Herzschuh, U.: Spatial variability of Holocene changes in
1071 the annual precipitation pattern: a model-data synthesis for the Asian monsoon region, *Climate*
1072 *Dynamics*, 40, 2919-2936, <https://doi.org/10.1007/s00382-012-1550-6>, 2013.
- 1073 Dallmeyer, A., Claussen, M., Fischer, N., Haberkorn, K., Wagner, S., Pfeiffer, M., Jin, L., Khon, V.,
1074 Wang, Y., and Herzschuh, U.: The evolution of sub-monsoon systems in the Afro-Asian monsoon region
1075 during the Holocene – comparison of different transient climate model simulations, *Clim. Past*,
1076 11, 305-326, <https://doi.org/10.5194/cp-11-305-2015>, 2015.
- 1077 Davies, B. J., Hambrey, M. J., Smellie, J. L., Carrivick, J. L., and Glasser, N. F.: Antarctic Peninsula Ice
1078 Sheet evolution during the Cenozoic Era, *Quaternary Science Reviews*, 31, 30-66,
1079 <https://doi.org/10.1016/j.quascirev.2011.10.012>, 2012.
- 1080 de Vernal, A., Gersonde, R., Goosse, H., Seidenkrantz, M.-S., and Wolff, E. W.: Sea ice in the
1081 paleoclimate system: the challenge of reconstructing sea ice from proxies – an introduction, *Quaternary*
1082 *Science Reviews*, 79, 1-8, <https://doi.org/10.1016/j.quascirev.2013.08.009>, 2013.
- 1083 Deacon, G.: The hydrography of the southern ocean, *Discovery Rep.*, 15, 1-124, 1937.
- 1084 DeConto, R. M. and Pollard, D.: Contribution of Antarctica to past and future sea-level rise, *Nature*, 531,
1085 591-597, <https://doi.org/10.1038/nature17145>, 2016.
- 1086 Denis, D., Crosta, X., Barbara, L., Massé, G., Renssen, H., Ther, O., and Giraudeau, J.: Sea ice and
1087 wind variability during the Holocene in East Antarctica: insight on middle–high latitude coupling,
1088 *Quaternary Science Reviews*, 29, 3709-3719, <https://doi.org/10.1016/j.quascirev.2010.08.007>, 2010.
- 1089 Denton, G. H., Anderson, R. F., Toggweiler, J. R., Edwards, R. L., Schaefer, J. M., and Putnam, A. E.:
1090 The Last Glacial Termination, *Science*, 328, 1652-1656, <https://doi.org/10.1126/science.1184119>,
1091 2010.
- 1092 Dickens, W. A., Graham, A. G. C., Smith, J. A., Dowdeswell, J. A., Larter, R. D., Hillenbrand, C.-D.,
1093 Trathan, P. N., Erik Arndt, J., and Kuhn, G.: A new bathymetric compilation for the South Orkney Islands
1094 region, Antarctic Peninsula (49°–39°W to 64°–59°S): Insights into the glacial development of the
1095 continental shelf, *Geochemistry, Geophysics, Geosystems*, 15, 2494-2514,
1096 <https://doi.org/10.1002/2014GC005323>, 2014.

- 1097 Dieckmann, G. S. and Hellmer, H. H.: The importance of sea ice: an overview, in: Sea ice, edited by:
1098 Dieckmann, G. S., and Hellmer, H. H., Blackwell Science Ltd, 1-22, 2010.
- 1099 Dorschel, B.: The Expedition PS118 of the Research Vessel POLARSTERN to the Weddell Sea in
1100 2019, Alfred Wegener Institute for Polar and Marine Research, Bremerhaven,
1101 https://doi.org/10.2312/BzPM_0735_2019, 2019.
- 1102 Ebert, E. E., Schramm, J. L., and Curry, J. A.: Disposition of solar radiation in sea ice and the upper
1103 ocean, *Journal of Geophysical Research: Oceans*, 100, 15965-15975,
1104 <https://doi.org/10.1029/95JC01672>, 1995.
- 1105 Elling, F. J., Könneke, M., Mußmann, M., Greve, A., and Hinrichs, K.-U.: Influence of temperature, pH,
1106 and salinity on membrane lipid composition and TEX₈₆ of marine planktonic thaumarchaeal isolates,
1107 *Geochimica et Cosmochimica Acta*, 171, 238-255, <https://doi.org/10.1016/j.gca.2015.09.004>, 2015.
- 1108 Elling, F. J., Könneke, M., Lipp, J. S., Becker, K. W., Gagen, E. J., and Hinrichs, K.-U.: Effects of growth
1109 phase on the membrane lipid composition of the thaumarchaeon *Nitrosopumilus maritimus* and their
1110 implications for archaeal lipid distributions in the marine environment, *Geochimica et Cosmochimica*
1111 *Acta*, 141, 579-597, <https://doi.org/10.1016/j.gca.2014.07.005>, 2014.
- 1112 EPICA Community Members: One-to-one coupling of glacial climate variability in Greenland and
1113 Antarctica, *Nature*, 444, 195-198, <https://doi.org/10.1038/nature05301>, 2006.
- 1114 Esper, O. and Gersonde, R.: Quaternary surface water temperature estimations: New diatom transfer
1115 functions for the Southern Ocean, *Palaeogeography, Palaeoclimatology, Palaeoecology*, 414, 1-19,
1116 <https://doi.org/10.1016/j.palaeo.2014.08.008>, 2014a.
- 1117 Esper, O. and Gersonde, R.: New tools for the reconstruction of Pleistocene Antarctic sea ice,
1118 *Palaeogeography, Palaeoclimatology, Palaeoecology*, 399, 260-283,
1119 <https://doi.org/10.1016/j.palaeo.2014.01.019>, 2014b.
- 1120 Etourneau, J., Collins, L. G., Willmott, V., Kim, J. H., Barbara, L., Leventer, A., Schouten, S., Sinninghe
1121 Damsté, J. S., Bianchini, A., Klein, V., Crosta, X., and Massé, G.: Holocene climate variations in the
1122 western Antarctic Peninsula: evidence for sea ice extent predominantly controlled by changes in
1123 insolation and ENSO variability, *Clim. Past*, 9, 1431-1446, <https://doi.org/10.5194/cp-9-1431-2013>,
1124 2013.
- 1125 Fahrbach, E., Rohardt, G., and Krause, G.: The Antarctic coastal current in the southeastern Weddell
1126 Sea, *Polar Biology*, 12, 171-182, <https://doi.org/10.1007/BF00238257>, 1992.
- 1127 Fedotova, A. A. and Stepanova, S. V.: Water Mass Transformation in the Powell Basin, in: Antarctic
1128 Peninsula Region of the Southern Ocean: Oceanography and Ecology, edited by: Morozov, E. G., Flint,
1129 M. V., and Spiridonov, V. A., Springer International Publishing, Cham, 115-129,
1130 https://doi.org/10.1007/978-3-030-78927-5_8, 2021.
- 1131 Ferrari, R., Jansen, M. F., Adkins, J. F., Burke, A., Stewart, A. L., and Thompson, A. F.: Antarctic sea
1132 ice control on ocean circulation in present and glacial climates, *Proceedings of the National Academy*
1133 *of Sciences*, 111, 8753-8758, <https://doi.org/10.1073/pnas.1323922111>, 2014.
- 1134 Fietz, S., Ho, S. L., and Huguet, C.: Archaeal Membrane Lipid-Based Paleothermometry for
1135 Applications in Polar Oceans, *Oceanography*, 33, 104-114, <https://www.jstor.org/stable/26937748>,
1136 2020.
- 1137 Fischer, H., Fundel, F., Ruth, U., Twarloh, B., Wegner, A., Udisti, R., Becagli, S., Castellano, E.,
1138 Morganti, A., Severi, M., Wolff, E., Littot, G., Röthlisberger, R., Mulvaney, R., Hutterli, M. A., Kaufmann,
1139 P., Federer, U., Lambert, F., Bigler, M., Hansson, M., Jonsell, U., de Angelis, M., Boutron, C., Siggaard-
1140 Andersen, M.-L., Steffensen, J. P., Barbante, C., Gaspari, V., Gabrielli, P., and Wagenbach, D.:
1141 Reconstruction of millennial changes in dust emission, transport and regional sea ice coverage using
1142 the deep EPICA ice cores from the Atlantic and Indian Ocean sector of Antarctica, *Earth and Planetary*
1143 *Science Letters*, 260, 340-354, <https://doi.org/10.1016/j.epsl.2007.06.014>, 2007.

- 1144 Geibert, W., Stimac, I., Rutgers Van Der Loeff, M., and Kuhn, G.: Dating Deep-Sea Sediments With
 1145 ²³⁰Th Excess Using a Constant Rate of Supply Model, *Paleoceanography and Paleoclimatology*, 34,
 1146 1895-1912, <https://doi.org/10.1029/2019PA003663>, 2019.
- 1147 Gersonde, R. and Zielinski, U.: The reconstruction of late Quaternary Antarctic sea-ice distribution—
 1148 the use of diatoms as a proxy for sea-ice, *Palaeogeography, Palaeoclimatology, Palaeoecology*, 162,
 1149 263-286, [https://doi.org/10.1016/S0031-0182\(00\)00131-0](https://doi.org/10.1016/S0031-0182(00)00131-0), 2000.
- 1150 Gersonde, R., Crosta, X., Abelmann, A., and Armand, L.: Sea-surface temperature and sea ice
 1151 distribution of the Southern Ocean at the EPILOG Last Glacial Maximum—a circum-Antarctic view
 1152 based on siliceous microfossil records, *Quaternary Science Reviews*, 24, 869-896,
 1153 <https://doi.org/10.1016/j.quascirev.2004.07.015>, 2005.
- 1154 Gersonde, R., Abelmann, A., Brathauer, U., Becquey, S., Bianchi, C., Cortese, G., Grobe, H., Kuhn, G.,
 1155 Niebler, H.-S., Segl, M., Sieger, R., Zielinski, U., and Fütterer, D. K.: Last glacial sea surface
 1156 temperatures and sea-ice extent in the Southern Ocean (Atlantic-Indian sector): A multiproxy approach,
 1157 *Paleoceanography*, 18, <https://doi.org/10.1029/2002PA000809>, 2003.
- 1158 Goelzer, H., Huybrechts, P., Loutre, M. F., and Fichet, T.: Last Interglacial climate and sea-level
 1159 evolution from a coupled ice sheet–climate model, *Clim. Past*, 12, 2195-2213,
 1160 <https://doi.org/10.5194/cp-12-2195-2016>, 2016.
- 1161 Gordon, A. L., Visbeck, M., and Huber, B.: Export of Weddell Sea deep and bottom water, *Journal of*
 1162 *Geophysical Research: Oceans*, 106, 9005-9017, <https://doi.org/10.1029/2000JC000281>, 2001.
- 1163 Greene, C. A., Young, D. A., Gwyther, D. E., Galton-Fenzi, B. K., and Blankenship, D. D.: Seasonal
 1164 dynamics of Totten Ice Shelf controlled by sea ice buttressing, *The Cryosphere*, 12, 2869-2882,
 1165 <https://doi.org/10.5194/tc-12-2869-2018>, 2018.
- 1166 Guagnin, M., Jennings, R., Eager, H., Parton, A., Stimpson, C., Stepanek, C., Pfeiffer, M., Groucutt, H.
 1167 S., Drake, N. A., Alsharekh, A., and Petraglia, M. D.: Rock art imagery as a proxy for Holocene
 1168 environmental change: A view from Shuwaymis, NW Saudi Arabia, *The Holocene*, 26, 1822-1834,
 1169 <https://doi.org/10.1177/0959683616645949>, 2016.
- 1170 Hagemann, J. R., Lembke-Jene, L., Lamy, F., Vorrath, M. E., Kaiser, J., Müller, J., Arz, H. W., Hefter,
 1171 J., Jaeschke, A., Ruggieri, N., and Tiedemann, R.: Upper-ocean temperature characteristics in the
 1172 subantarctic southeastern Pacific based on biomarker reconstructions, *Clim. Past*, 19, 1825-1845,
 1173 <https://doi.org/10.5194/cp-19-1825-2023>, 2023.
- 1174 Haywood, A. M., Hill, D. J., Dolan, A. M., Otto-Bliesner, B. L., Bragg, F., Chan, W. L., Chandler, M. A.,
 1175 Contoux, C., Dowsett, H. J., Jost, A., Kamae, Y., Lohmann, G., Lunt, D. J., Abe-Ouchi, A., Pickering,
 1176 S. J., Ramstein, G., Rosenbloom, N. A., Salzmann, U., Sohl, L., Stepanek, C., Ueda, H., Yan, Q., and
 1177 Zhang, Z.: Large-scale features of Pliocene climate: results from the Pliocene Model Intercomparison
 1178 Project, *Clim. Past*, 9, 191-209, <https://doi.org/10.5194/cp-9-191-2013>, 2013.
- 1179 Heroy, D. C., Sjunneskog, C., and Anderson, J. B.: Holocene climate change in the Bransfield Basin,
 1180 Antarctic Peninsula: evidence from sediment and diatom analysis, *Antarctic Science*, 20, 69-87,
 1181 <https://doi.org/10.1017/S0954102007000788>, 2008.
- 1182 Herron, M. J. and Anderson, J. B.: Late quaternary glacial history of the South Orkney Plateau,
 1183 Antarctica, *Quaternary Research*, 33, 265-275, [https://doi.org/10.1016/0033-5894\(90\)90055-P](https://doi.org/10.1016/0033-5894(90)90055-P), 1990.
- 1184 Hibler, W. D.: A Dynamic Thermodynamic Sea Ice Model, *Journal of Physical Oceanography*, 9, 815-
 1185 846, [https://doi.org/10.1175/1520-0485\(1979\)009<0815:ADTSIM>2.0.CO;2](https://doi.org/10.1175/1520-0485(1979)009<0815:ADTSIM>2.0.CO;2), 1979.
- 1186 Hoffman, J. S., Clark, P. U., Parnell, A. C., and He, F.: Regional and global sea-surface temperatures
 1187 during the last interglaciation, *Science*, 355, 276-279, <https://doi.org/10.1126/science.aai8464>, 2017.

- 1188 Holloway, M. D., Sime, L. C., Singarayer, J. S., Tindall, J. C., Bunch, P., and Valdes, P. J.: Antarctic
 1189 last interglacial isotope peak in response to sea ice retreat not ice-sheet collapse, *Nature*
 1190 *Communications*, 7, 12293, <https://doi.org/10.1038/ncomms12293>, 2016.
- 1191 Holloway, M. D., Sime, L. C., Allen, C. S., Hillenbrand, C. D., Bunch, P., Wolff, E., and Valdes, P. J.:
 1192 The spatial structure of the 128 ka Antarctic sea ice minimum, *Geophysical Research Letters*, 44,
 1193 11,129-111,139, <https://doi.org/10.1002/2017GL074594>, 2017.
- 1194 Hopmans, E. C., Weijers, J. W. H., Schefuß, E., Herfort, L., Sinninghe Damsté, J. S., and Schouten, S.:
 1195 A novel proxy for terrestrial organic matter in sediments based on branched and isoprenoid tetraether
 1196 lipids, *Earth and Planetary Science Letters*, 224, 107-116, <https://doi.org/10.1016/j.epsl.2004.05.012>,
 1197 2004.
- 1198 Huhn, O., Hellmer, H. H., Rhein, M., Rodehacke, C., Roether, W., Schodlok, M. P., and Schröder, M.:
 1199 Evidence of deep- and bottom-water formation in the western Weddell Sea, *Deep Sea Research Part*
 1200 *II: Topical Studies in Oceanography*, 55, 1098-1116, <https://doi.org/10.1016/j.dsr2.2007.12.015>, 2008.
- 1201 Inglis, G. N., Farnsworth, A., Lunt, D., Foster, G. L., Hollis, C. J., Pagani, M., Jardine, P. E., Pearson,
 1202 P. N., Markwick, P., Galsworthy, A. M. J., Raynham, L., Taylor, K. W. R., and Pancost, R. D.: Descent
 1203 toward the Icehouse: Eocene sea surface cooling inferred from GDGT distributions, *Paleoceanography*,
 1204 30, 1000-1020, <https://doi.org/10.1002/2014PA002723>, 2015.
- 1205 Jacobs, S. S.: On the nature and significance of the Antarctic Slope Front, *Marine Chemistry*, 35, 9-24,
 1206 [https://doi.org/10.1016/S0304-4203\(09\)90005-6](https://doi.org/10.1016/S0304-4203(09)90005-6), 1991.
- 1207 Jennings, R. P., Singarayer, J., Stone, E. J., Krebs-Kanzow, U., Khon, V., Nisancioglu, K. H., Pfeiffer,
 1208 M., Zhang, X., Parker, A., Parton, A., Groucutt, H. S., White, T. S., Drake, N. A., and Petraglia, M. D.:
 1209 The greening of Arabia: Multiple opportunities for human occupation of the Arabian Peninsula during
 1210 the Late Pleistocene inferred from an ensemble of climate model simulations, *Quaternary International*,
 1211 382, 181-199, <https://doi.org/10.1016/j.quaint.2015.01.006>, 2015.
- 1212 Johnson, R. G. and Andrews, J. T.: Glacial terminations in the oxygen isotope record of deep sea cores:
 1213 hypothesis of massive Antarctic ice-shelf destruction, *Palaeogeography, Palaeoclimatology,*
 1214 *Palaeoecology*, 53, 107-138, [https://doi.org/10.1016/0031-0182\(86\)90041-6](https://doi.org/10.1016/0031-0182(86)90041-6), 1986.
- 1215 Jungclauss, J. H., Keenlyside, N., Botzet, M., Haak, H., Luo, J.-J., Latif, M., Marotzke, J., Mikolajewicz,
 1216 U., and Roeckner, E.: Ocean Circulation and Tropical Variability in the Coupled Model ECHAM5/MP1-
 1217 OM, *Journal of Climate*, 19, 3952-3972, <https://doi.org/10.1175/JCLI3827.1>, 2006.
- 1218 Khoo, W. W., Esper, O., Xiao, W., Hefter, J., and Müller, J.: Sea-ice distribution and ocean temperature
 1219 variation in the Powell Basin and Scotia Sea, inferred from marine sediment cores PS118_63-1 and
 1220 PS67/219-1, PANGAEA [dataset], <https://doi.org/10.1594/PANGAEA.965042>, 2024.
- 1221 Kim, J.-H., Crosta, X., Willmott, V., Renssen, H., Bonnin, J., Helmke, P., Schouten, S., and Sinninghe
 1222 Damsté, J. S.: Holocene subsurface temperature variability in the eastern Antarctic continental margin,
 1223 *Geophysical Research Letters*, 39, <https://doi.org/10.1029/2012GL051157>, 2012.
- 1224 Kim, J.-H., van der Meer, J., Schouten, S., Helmke, P., Willmott, V., Sangiorgi, F., Koç, N., Hopmans,
 1225 E. C., and Damsté, J. S. S.: New indices and calibrations derived from the distribution of crenarchaeal
 1226 isoprenoid tetraether lipids: Implications for past sea surface temperature reconstructions, *Geochimica*
 1227 *et Cosmochimica Acta*, 74, 4639-4654, <https://doi.org/10.1016/j.gca.2010.05.027>, 2010.
- 1228 Klein, K., Weniger, G.-C., Ludwig, P., Stepanek, C., Zhang, X., Wegener, C., and Shao, Y.: Assessing
 1229 climatic impact on transition from Neanderthal to anatomically modern human population on Iberian
 1230 Peninsula: a macroscopic perspective, *Science Bulletin*, 68, 1176-1186,
 1231 <https://doi.org/10.1016/j.scib.2023.04.025>, 2023.
- 1232 Lambeck, K., Purcell, A., Zhao, J., and Svensson, N.-O.: The Scandinavian Ice Sheet: from MIS 4 to
 1233 the end of the Last Glacial Maximum, *Boreas*, 39, 410-435, <https://doi.org/10.1111/j.1502-3885.2010.00140.x>, 2010.

- 1235 Lamping, N., Müller, J., Esper, O., Hillenbrand, C.-D., Smith, J. A., and Kuhn, G.: Highly branched
 1236 isoprenoids reveal onset of deglaciation followed by dynamic sea-ice conditions in the western
 1237 Amundsen Sea, Antarctica, *Quaternary Science Reviews*, 228, 106103,
 1238 <https://doi.org/10.1016/j.quascirev.2019.106103>, 2020.
- 1239 Lamping, N., Müller, J., Hefter, J., Mollenhauer, G., Haas, C., Shi, X., Vorrath, M. E., Lohmann, G., and
 1240 Hillenbrand, C. D.: Evaluation of lipid biomarkers as proxies for sea ice and ocean temperatures along
 1241 the Antarctic continental margin, *Clim. Past*, 17, 2305-2326, <https://doi.org/10.5194/cp-17-2305-2021>,
 1242 2021.
- 1243 Laskar, J., Robutel, P., Joutel, F., Gastineau, M., Correia, A. C. M., and Levrard, B.: A long-term
 1244 numerical solution for the insolation quantities of the Earth, *A&A*, 428, 261-285,
 1245 <https://doi.org/10.1051/0004-6361:20041335>, 2004.
- 1246 Lee, J. I., Bak, Y.-S., Yoo, K.-C., Lim, H. S., Yoon, H. I., and Yoon, S. H.: Climate changes in the South
 1247 Orkney Plateau during the last 8600 years, *The Holocene*, 20, 395-404,
 1248 <https://doi.org/10.1177/0959683609353430>, 2010.
- 1249 Leventer, A.: The fate of Antarctic "sea ice diatoms" and their use as paleoenvironmental indicators,
 1250 *Antarctic sea ice: biological processes, interactions and variability*, 73, 121-137, 1998.
- 1251 Liu, R., Han, Z., Zhao, J., Zhang, H., Li, D., Ren, J., Pan, J., and Zhang, H.: Distribution and source of
 1252 glycerol dialkyl glycerol tetraethers (GDGTs) and the applicability of GDGT-based temperature proxies
 1253 in surface sediments of Prydz Bay, East Antarctica, *Polar Research*, 39,
 1254 <https://doi.org/10.33265/polar.v39.3557>, 2020.
- 1255 Liu, X.-L., Summons, R. E., and Hinrichs, K.-U.: Extending the known range of glycerol ether lipids in
 1256 the environment: structural assignments based on tandem mass spectral fragmentation patterns, *Rapid*
 1257 *Communications in Mass Spectrometry*, 26, 2295-2302, <https://doi.org/10.1002/rcm.6355>, 2012a.
- 1258 Liu, X.-L., Lipp, J. S., Simpson, J. H., Lin, Y.-S., Summons, R. E., and Hinrichs, K.-U.: Mono- and
 1259 dihydroxyl glycerol dibiphytanyl glycerol tetraethers in marine sediments: Identification of both core and
 1260 intact polar lipid forms, *Geochimica et Cosmochimica Acta*, 89, 102-115,
 1261 <https://doi.org/10.1016/j.gca.2012.04.053>, 2012b.
- 1262 Locarnini, R. A., Mishonov, A. V., Baranova, O. K., Boyer, T. P., Zweng, M. M., Garcia, H. E., Reagan,
 1263 J. R., Seidov, D., Weathers, K., Paver, C. R., and Smolyar, I.: *World Ocean Atlas 2018, Volume 1:*
 1264 *Temperature [dataset]*, 2018.
- 1265 Loveland, T. R., Reed, B. C., Brown, J. F., Ohlen, D. O., Zhu, Z., Yang, L., and Merchant, J. W.:
 1266 Development of a global land cover characteristics database and IGBP DISCover from 1 km AVHRR
 1267 data, *International Journal of Remote Sensing*, 21, 1303-1330,
 1268 <https://doi.org/10.1080/014311600210191>, 2000.
- 1269 Lü, X., Liu, X.-L., Elling, F. J., Yang, H., Xie, S., Song, J., Li, X., Yuan, H., Li, N., and Hinrichs, K.-U.:
 1270 Hydroxylated isoprenoid GDGTs in Chinese coastal seas and their potential as a paleotemperature
 1271 proxy for mid-to-low latitude marginal seas, *Organic Geochemistry*, 89-90, 31-43,
 1272 <https://doi.org/10.1016/j.orggeochem.2015.10.004>, 2015.
- 1273 Lunt, D. J., Abe-Ouchi, A., Bakker, P., Berger, A., Braconnot, P., Charbit, S., Fischer, N., Herold, N.,
 1274 Jungclauss, J. H., Khon, V. C., Krebs-Kanzow, U., Langebroek, P. M., Lohmann, G., Nisancioglu, K. H.,
 1275 Otto-Bliessner, B. L., Park, W., Pfeiffer, M., Phipps, S. J., Prange, M., Rachmayani, R., Renssen, H.,
 1276 Rosenbloom, N., Schneider, B., Stone, E. J., Takahashi, K., Wei, W., Yin, Q., and Zhang, Z. S.: A multi-
 1277 model assessment of last interglacial temperatures, *Clim. Past*, 9, 699-717, [https://doi.org/10.5194/cp-](https://doi.org/10.5194/cp-9-699-2013)
 1278 [9-699-2013](https://doi.org/10.5194/cp-9-699-2013), 2013.
- 1279 Luo, F., Ying, J., Liu, T., and Chen, D.: Origins of Southern Ocean warm sea surface temperature bias
 1280 in CMIP6 models, *npj Climate and Atmospheric Science*, 6, 127, [https://doi.org/10.1038/s41612-023-](https://doi.org/10.1038/s41612-023-00456-6)
 1281 [00456-6](https://doi.org/10.1038/s41612-023-00456-6), 2023.

- 1282 Marino, G., Rohling, E. J., Rodríguez-Sanz, L., Grant, K. M., Heslop, D., Roberts, A. P., Stanford, J. D.,
1283 and Yu, J.: Bipolar seesaw control on last interglacial sea level, *Nature*, 522, 197-201,
1284 <https://doi.org/10.1038/nature14499>, 2015.
- 1285 Marsland, S. J., Haak, H., Jungclauss, J. H., Latif, M., and Röske, F.: The Max-Planck-Institute global
1286 ocean/sea ice model with orthogonal curvilinear coordinates, *Ocean Modelling*, 5, 91-127,
1287 [https://doi.org/10.1016/S1463-5003\(02\)00015-X](https://doi.org/10.1016/S1463-5003(02)00015-X), 2003.
- 1288 Massé, G., Belt, S. T., Crosta, X., Schmidt, S., Snape, I., Thomas, D. N., and Rowland, S. J.: Highly
1289 branched isoprenoids as proxies for variable sea ice conditions in the Southern Ocean, *Antarctic*
1290 *Science*, 23, 487-498, <https://doi.org/10.1017/S0954102011000381>, 2011.
- 1291 Massom, R. A., Scambos, T. A., Bennetts, L. G., Reid, P., Squire, V. A., and Stammerjohn, S. E.:
1292 Antarctic ice shelf disintegration triggered by sea ice loss and ocean swell, *Nature*, 558, 383-389,
1293 <https://doi.org/10.1038/s41586-018-0212-1>, 2018.
- 1294 Massom, R. A., Giles, A. B., Warner, R. C., Fricker, H. A., Legrésy, B., Hyland, G., Lescarmonier, L.,
1295 and Young, N.: External influences on the Mertz Glacier Tongue (East Antarctica) in the decade leading
1296 up to its calving in 2010, *Journal of Geophysical Research: Earth Surface*, 120, 490-506,
1297 <https://doi.org/10.1002/2014JF003223>, 2015.
- 1298 Masson-Delmotte, V., Buiron, D., Ekaykin, A., Frezzotti, M., Gallée, H., Jouzel, J., Krinner, G., Landais,
1299 A., Motoyama, H., Oerter, H., Pol, K., Pollard, D., Ritz, C., Schlosser, E., Sime, L. C., Sodemann, H.,
1300 Stenni, B., Uemura, R., and Vimeux, F.: A comparison of the present and last interglacial periods in six
1301 Antarctic ice cores, *Clim. Past*, 7, 397-423, <https://doi.org/10.5194/cp-7-397-2011>, 2011.
- 1302 Morozov, E. G., Frey, D. I., and Tarakanov, R. Y.: Antarctic Bottom Water Flow through the Eastern
1303 Part of the Philip Passage in the Weddell Sea, *Oceanology*, 60, 589-592,
1304 <https://doi.org/10.1134/S000143702005015X>, 2020.
- 1305 Müller, J., Wagner, A., Fahl, K., Stein, R., Prange, M., and Lohmann, G.: Towards quantitative sea ice
1306 reconstructions in the northern North Atlantic: A combined biomarker and numerical modelling
1307 approach, *Earth and Planetary Science Letters*, 306, 137-148,
1308 <https://doi.org/10.1016/j.epsl.2011.04.011>, 2011.
- 1309 Müller, P. J. and Schneider, R.: An automated leaching method for the determination of opal in
1310 sediments and particulate matter, *Deep Sea Research Part I: Oceanographic Research Papers*, 40,
1311 425-444, 1993.
- 1312 Naughten, K. A., Meissner, K. J., Galton-Fenzi, B. K., England, M. H., Timmermann, R., Hellmer, H. H.,
1313 Hattermann, T., and Debernard, J. B.: Intercomparison of Antarctic ice-shelf, ocean, and sea-ice
1314 interactions simulated by MetROMS-iceshelf and FESOM 1.4, *Geosci. Model Dev.*, 11, 1257-1292,
1315 <https://doi.org/10.5194/gmd-11-1257-2018>, 2018.
- 1316 Naveira Garabato, A. C., McDonagh, E. L., Stevens, D. P., Heywood, K. J., and Sanders, R. J.: On the
1317 export of Antarctic Bottom Water from the Weddell Sea, *Deep Sea Research Part II: Topical Studies in*
1318 *Oceanography*, 49, 4715-4742, [https://doi.org/10.1016/S0967-0645\(02\)00156-X](https://doi.org/10.1016/S0967-0645(02)00156-X), 2002.
- 1319 Ó Cofaigh, C., Davies, B. J., Livingstone, S. J., Smith, J. A., Johnson, J. S., Hocking, E. P., Hodgson,
1320 D. A., Anderson, J. B., Bentley, M. J., Canals, M., Domack, E., Dowdeswell, J. A., Evans, J., Glasser,
1321 N. F., Hillenbrand, C.-D., Larter, R. D., Roberts, S. J., and Simms, A. R.: Reconstruction of ice-sheet
1322 changes in the Antarctic Peninsula since the Last Glacial Maximum, *Quaternary Science Reviews*, 100,
1323 87-110, <https://doi.org/10.1016/j.quascirev.2014.06.023>, 2014.
- 1324 Olbers, D., Gouretsky, V., Seiss, G., and Schröter, J.: Hydrographic atlas of the Southern Ocean, Alfred-
1325 Wegener-Institut, Bremerhaven 1992.
- 1326 Orsi, A. H., Johnson, G. C., and Bullister, J. L.: Circulation, mixing, and production of Antarctic Bottom
1327 Water, *Progress in Oceanography*, 43, 55-109, [https://doi.org/10.1016/S0079-6611\(99\)00004-X](https://doi.org/10.1016/S0079-6611(99)00004-X), 1999.

- 1328 Orsi, A. H., Nowlin, W. D., and Whitworth, T.: On the circulation and stratification of the Weddell Gyre,
1329 Deep Sea Research Part I: Oceanographic Research Papers, 40, 169-203,
1330 [https://doi.org/10.1016/0967-0637\(93\)90060-G](https://doi.org/10.1016/0967-0637(93)90060-G), 1993.
- 1331 Orsi, A. H., Whitworth, T., and Nowlin, W. D.: On the meridional extent and fronts of the Antarctic
1332 Circumpolar Current, Deep Sea Research Part I: Oceanographic Research Papers, 42, 641-673,
1333 [https://doi.org/10.1016/0967-0637\(95\)00021-W](https://doi.org/10.1016/0967-0637(95)00021-W), 1995.
- 1334 Otto-Bliesner, B. L., Rosenbloom, N., Stone, E. J., McKay, N. P., Lunt, D. J., Brady, E. C., and
1335 Overpeck, J. T.: How warm was the last interglacial? New model–data comparisons, Philosophical
1336 Transactions of the Royal Society A: Mathematical, Physical and Engineering Sciences, 371,
1337 20130097, <https://doi.org/10.1098/rsta.2013.0097>, 2013.
- 1338 Otto-Bliesner, B. L., Braconnot, P., Harrison, S. P., Lunt, D. J., Abe-Ouchi, A., Albani, S., Bartlein, P.
1339 J., Capron, E., Carlson, A. E., Dutton, A., Fischer, H., Goelzer, H., Govin, A., Haywood, A., Joos, F.,
1340 LeGrande, A. N., Lipscomb, W. H., Lohmann, G., Mahowald, N., Nehrbaas-Ahles, C., Pausata, F. S.
1341 R., Peterschmitt, J. Y., Phipps, S. J., Renssen, H., and Zhang, Q.: The PMIP4 contribution to CMIP6 –
1342 Part 2: Two interglacials, scientific objective and experimental design for Holocene and Last Interglacial
1343 simulations, Geosci. Model Dev., 10, 3979-4003, <https://doi.org/10.5194/gmd-10-3979-2017>, 2017.
- 1344 Park, E., Hefter, J., Fischer, G., Iversen, M. H., Ramondenc, S., Nöthig, E. M., and Mollenhauer, G.:
1345 Seasonality of archaeal lipid flux and GDGT-based thermometry in sinking particles of high-latitude
1346 oceans: Fram Strait (79°N) and Antarctic Polar Front (50°S), Biogeosciences, 16, 2247-2268,
1347 <https://doi.org/10.5194/bg-16-2247-2019>, 2019.
- 1348 Pedro, J. B., van Ommen, T. D., Rasmussen, S. O., Morgan, V. I., Chappellaz, J., Moy, A. D., Masson-
1349 Delmotte, V., and Delmotte, M.: The last deglaciation: timing the bipolar seesaw, Clim. Past, 7, 671-
1350 683, <https://doi.org/10.5194/cp-7-671-2011>, 2011.
- 1351 Pedro, J. B., Bostock, H. C., Bitz, C. M., He, F., Vandergoes, M. J., Steig, E. J., Chase, B. M., Krause,
1352 C. E., Rasmussen, S. O., Markle, B. R., and Cortese, G.: The spatial extent and dynamics of the
1353 Antarctic Cold Reversal, Nature Geoscience, 9, 51-55, <https://doi.org/10.1038/ngeo2580>, 2016.
- 1354 Pellichero, V., Sallée, J.-B., Chapman, C. C., and Downes, S. M.: The southern ocean meridional
1355 overturning in the sea-ice sector is driven by freshwater fluxes, Nature Communications, 9, 1789,
1356 <https://doi.org/10.1038/s41467-018-04101-2>, 2018.
- 1357 Pfeiffer, M. and Lohmann, G.: Greenland Ice Sheet influence on Last Interglacial climate: global
1358 sensitivity studies performed with an atmosphere–ocean general circulation model, Clim. Past, 12,
1359 1313-1338, <https://doi.org/10.5194/cp-12-1313-2016>, 2016.
- 1360 Pitcher, A., Hopmans, E. C., Mosier, A. C., Park, S. J., Rhee, S. K., Francis, C. A., Schouten, S., and
1361 Sinninghe Damsté, J. S.: Core and intact polar glycerol dibiphytanyl glycerol tetraether lipids of
1362 ammonia-oxidizing Archaea enriched from marine and estuarine sediments, Applied and Environmental
1363 Microbiology, 77, 3468-3477, <https://doi.org/10.1128/AEM.02758-10>, 2011.
- 1364 Pollard, D. and DeConto, R. M.: Modelling West Antarctic ice sheet growth and collapse through the
1365 past five million years, Nature, 458, 329-332, <https://doi.org/10.1038/nature07809>, 2009.
- 1366 Raddatz, T. J., Reick, C. H., Knorr, W., Kattge, J., Roeckner, E., Schnur, R., Schnitzler, K. G., Wetzel,
1367 P., and Jungclauss, J.: Will the tropical land biosphere dominate the climate–carbon cycle feedback
1368 during the twenty-first century?, Climate Dynamics, 29, 565-574, <https://doi.org/10.1007/s00382-007-0247-8>, 2007.
- 1370 Reynolds, R. W., Rayner, N. A., Smith, T. M., Stokes, D. C., and Wang, W.: An Improved In Situ and
1371 Satellite SST Analysis for Climate, Journal of Climate, 15, 1609-1625, [https://doi.org/10.1175/1520-0442\(2002\)015](https://doi.org/10.1175/1520-0442(2002)015)
1372 [0442\(2002\)015](https://doi.org/10.1175/1520-0442(2002)015)<1609:AIISAS>2.0.CO;2, 2002.

- 1373 Reynolds, R. W., Smith, T. M., Liu, C., Chelton, D. B., Casey, K. S., and Schlax, M. G.: Daily High-
 1374 Resolution-Blended Analyses for Sea Surface Temperature, *Journal of Climate*, 20, 5473-5496,
 1375 <https://doi.org/10.1175/2007JCLI1824.1>, 2007.
- 1376 Rhodes, R., Kohfeld, K., Bostock, H., Crosta, X., Leventer, A., Meissner, K., and Esper, O.:
 1377 Understanding past changes in sea ice in the Southern Ocean, *Past Global Changes Magazine*, 27(1),
 1378 31, <https://doi.org/10.22498/pages.27.1.31>, 2019.
- 1379 Riaux-Gobin, C. and Poulin, M.: Possible symbiosis of *Berkeleya adeliensis* Medlin, *Synedropsis fragilis*
 1380 (Manguin) Hasle et al. and *Nitzschia lecontei* Van Heurck (Bacillariophyta) associated with land-fast
 1381 ice in Adélie Land, Antarctica, *Diatom Research*, 19, 265-274, 2004.
- 1382 Rintoul, S. R.: The global influence of localized dynamics in the Southern Ocean, *Nature*, 558, 209-218,
 1383 <https://doi.org/10.1038/s41586-018-0182-3>, 2018.
- 1384 Robel, A. A.: Thinning sea ice weakens buttressing force of iceberg mélange and promotes calving,
 1385 *Nature Communications*, 8, 14596, <https://doi.org/10.1038/ncomms14596>, 2017.
- 1386 Rohling, E. J., Hibbert, F. D., Williams, F. H., Grant, K. M., Marino, G., Foster, G. L., Hennekam, R., de
 1387 Lange, G. J., Roberts, A. P., Yu, J., Webster, J. M., and Yokoyama, Y.: Differences between the last
 1388 two glacial maxima and implications for ice-sheet, $\delta^{18}\text{O}$, and sea-level reconstructions, *Quaternary*
 1389 *Science Reviews*, 176, 1-28, <https://doi.org/10.1016/j.quascirev.2017.09.009>, 2017.
- 1390 Ryves, D. B., Battarbee, R. W., and Fritz, S. C.: The dilemma of disappearing diatoms: Incorporating
 1391 diatom dissolution data into palaeoenvironmental modelling and reconstruction, *Quaternary Science*
 1392 *Reviews*, 28, 120-136, <https://doi.org/10.1016/j.quascirev.2008.08.021>, 2009.
- 1393 Sadatzki, H., Opdyke, B., Menviel, L., Leventer, A., Hope, J. M., Brocks, J. J., Fallon, S., Post, A. L.,
 1394 O'Brien, P. E., Grant, K., and Armand, L.: Early sea ice decline off East Antarctica at the last glacial–
 1395 interglacial climate transition, *Science Advances*, 9, eadh9513, <https://doi.org/10.1126/sciadv.adh9513>,
 1396 2023.
- 1397 Seabrooke, J. M., Hufford, G. L., and Elder, R. B.: Formation of Antarctic bottom water in the Weddell
 1398 Sea, *Journal of Geophysical Research* (1896-1977), 76, 2164-2178,
 1399 <https://doi.org/10.1029/JC076i009p02164>, 1971.
- 1400 Shevenell, A. E., Domack, E. W., and Kernan, G. M.: Record of Holocene palaeoclimate change along
 1401 the Antarctic Peninsula: evidence from glacial marine sediments, Lallemand Fjord, *Papers and*
 1402 *Proceedings of the Royal Society of Tasmania*, 55-64,
- 1403 Sinninghe Damsté, J. S., Rijpstra, W. I. C., Hopmans, E. C., Jung, J., Kim, J. H., Rhee, S. K.,
 1404 Stieglmeier, M., and Schleper, C.: Intact Polar and Core Glycerol Dibiphytanyl Glycerol Tetraether
 1405 Lipids of Group I.1a and I.1b Thaumarchaeota in Soil, *Applied and Environmental Microbiology*, 78,
 1406 6866-6874, <https://doi.org/10.1128/AEM.01681-12>, 2012.
- 1407 Smik, L., Belt, S. T., Lieser, J. L., Armand, L. K., and Leventer, A.: Distributions of highly branched
 1408 isoprenoid alkenes and other algal lipids in surface waters from East Antarctica: Further insights for
 1409 biomarker-based paleo sea-ice reconstruction, *Organic Geochemistry*, 95, 71-80,
 1410 <https://doi.org/10.1016/j.orggeochem.2016.02.011>, 2016.
- 1411 Stepanek, C. and Lohmann, G.: Modelling mid-Pliocene climate with COSMOS, *Geosci. Model Dev.*,
 1412 5, 1221-1243, <https://doi.org/10.5194/gmd-5-1221-2012>, 2012.
- 1413 Stepanek, C., Gierz, P., and Lohmann, G.: Simulated seasonal sea surface temperature, subsurface
 1414 ocean temperature, and sea ice distribution for selected periods of the last two glacial cycles,
 1415 PANGAEA [dataset], <https://doi.org/10.1594/PANGAEA.972654>, 2024.
- 1416 Stepanek, C., Samakinwa, E., Knorr, G., and Lohmann, G.: Contribution of the coupled atmosphere–
 1417 ocean–sea ice–vegetation model COSMOS to the Pliocene, *Clim. Past*, 16, 2275-2323,
 1418 <https://doi.org/10.5194/cp-16-2275-2020>, 2020.

- 1419 Stevens, B., Giorgetta, M., Esch, M., Mauritsen, T., Crueger, T., Rast, S., Salzmann, M., Schmidt, H.,
1420 Bader, J., Block, K., Brokopf, R., Fast, I., Kinne, S., Kornblueh, L., Lohmann, U., Pincus, R., Reichler,
1421 T., and Roeckner, E.: Atmospheric component of the MPI-M Earth System Model: ECHAM6, *Journal of*
1422 *Advances in Modeling Earth Systems*, 5, 146-172, <https://doi.org/10.1002/jame.20015>, 2013.
- 1423 Sutter, J., Gierz, P., Grosfeld, K., Thoma, M., and Lohmann, G.: Ocean temperature thresholds for Last
1424 Interglacial West Antarctic Ice Sheet collapse, *Geophysical Research Letters*, 43, 2675-2682,
1425 <https://doi.org/10.1002/2016GL067818>, 2016.
- 1426 Tarasov, L., Dyke, A. S., Neal, R. M., and Peltier, W. R.: A data-calibrated distribution of deglacial
1427 chronologies for the North American ice complex from glaciological modeling, *Earth and Planetary*
1428 *Science Letters*, 315-316, 30-40, <https://doi.org/10.1016/j.epsl.2011.09.010>, 2012.
- 1429 Taylor, F. and Sjunneskog, C.: Postglacial marine diatom record of the Palmer Deep, Antarctic
1430 Peninsula (ODP Leg 178, Site 1098) 2. Diatom assemblages, *Paleoceanography*, 17, PAL 2-1-PAL 2-
1431 12, <https://doi.org/10.1029/2000PA000564>, 2002.
- 1432 Taylor, F., Whitehead, J., and Domack, E.: Holocene paleoclimate change in the Antarctic Peninsula:
1433 evidence from the diatom, sedimentary and geochemical record, *Marine Micropaleontology*, 41, 25-43,
1434 [https://doi.org/10.1016/S0377-8398\(00\)00049-9](https://doi.org/10.1016/S0377-8398(00)00049-9), 2001.
- 1435 Thompson, A. F., Stewart, A. L., Spence, P., and Heywood, K. J.: The Antarctic Slope Current in a
1436 Changing Climate, *Reviews of Geophysics*, 56, 741-770, <https://doi.org/10.1029/2018RG000624>,
1437 2018.
- 1438 Turney, C. S. M., Fogwill, C. J., Golledge, N. R., McKay, N. P., van Sebille, E., Jones, R. T., Etheridge,
1439 D., Rubino, M., Thornton, D. P., Davies, S. M., Ramsey, C. B., Thomas, Z. A., Bird, M. I., Munksgaard,
1440 N. C., Kohno, M., Woodward, J., Winter, K., Weyrich, L. S., Rootes, C. M., Millman, H., Albert, P. G.,
1441 Rivera, A., van Ommen, T., Curran, M., Moy, A., Rahmstorf, S., Kawamura, K., Hillenbrand, C.-D.,
1442 Weber, M. E., Manning, C. J., Young, J., and Cooper, A.: Early Last Interglacial ocean warming drove
1443 substantial ice mass loss from Antarctica, *Proceedings of the National Academy of Sciences*, 117,
1444 3996-4006, <https://doi.org/10.1073/pnas.1902469117>, 2020.
- 1445 Varma, V., Prange, M., Merkel, U., Kleinen, T., Lohmann, G., Pfeiffer, M., Renssen, H., Wagner, A.,
1446 Wagner, S., and Schulz, M.: Holocene evolution of the Southern Hemisphere westerly winds in transient
1447 simulations with global climate models, *Clim. Past*, 8, 391-402, <https://doi.org/10.5194/cp-8-391-2012>,
1448 2012.
- 1449 Vaughan, D. G., Comiso, J. C., Allison, I., Carrasco, J., Kaser, G., Kwok, R., Mote, P., Murray, T., Paul,
1450 F., Ren, J., Rigno, E., Solomina, O., Steffen, K., and Zhang, T.: *Observations: Cryosphere*, Cambridge
1451 University Press, Cambridge, United Kingdom and New York, NY, USA, 2013.
- 1452 Vernet, M., Geibert, W., Hoppema, M., Brown, P. J., Haas, C., Hellmer, H. H., Jokat, W., Jullion, L.,
1453 Mazloff, M., Bakker, D. C. E., Brearley, J. A., Croot, P., Hattermann, T., Hauck, J., Hillenbrand, C.-D.,
1454 Hoppe, C. J. M., Huhn, O., Koch, B. P., Lechtenfeld, O. J., Meredith, M. P., Naveira Garabato, A. C.,
1455 Nöthig, E.-M., Peeken, I., Rutgers van der Loeff, M. M., Schmidtko, S., Schröder, M., Strass, V. H.,
1456 Torres-Valdés, S., and Verdy, A.: The Weddell Gyre, *Southern Ocean: Present Knowledge and Future*
1457 *Challenges*, *Reviews of Geophysics*, 57, 623-708, <https://doi.org/10.1029/2018RG000604>, 2019.
- 1458 Viseras, C. and Maldonado, A.: Facies architecture, seismic stratigraphy and development of a high-
1459 latitude basin: the Powell Basin (Antarctica), *Marine Geology*, 157, 69-87,
1460 [https://doi.org/10.1016/S0025-3227\(98\)00136-4](https://doi.org/10.1016/S0025-3227(98)00136-4), 1999.
- 1461 Vorrath, M. E., Müller, J., Esper, O., Mollenhauer, G., Haas, C., Schefuß, E., and Fahl, K.: Highly
1462 branched isoprenoids for Southern Ocean sea ice reconstructions: a pilot study from the Western
1463 Antarctic Peninsula, *Biogeosciences*, 16, 2961-2981, <https://doi.org/10.5194/bg-16-2961-2019>, 2019.
- 1464 Vorrath, M. E., Müller, J., Rebolledo, L., Cárdenas, P., Shi, X., Esper, O., Opel, T., Geibert, W., Muñoz,
1465 P., Haas, C., Kuhn, G., Lange, C. B., Lohmann, G., and Mollenhauer, G.: Sea ice dynamics in the

- 1466 Bransfield Strait, Antarctic Peninsula, during the past 240 years: a multi-proxy intercomparison study,
1467 *Clim. Past*, 16, 2459-2483, <https://doi.org/10.5194/cp-16-2459-2020>, 2020.
- 1468 Vorrath, M. E., Müller, J., Cárdenas, P., Opel, T., Mieruch, S., Esper, O., Lembke-Jene, L., Etourneau,
1469 J., Vieth-Hillebrand, A., Lahajnar, N., Lange, C. B., Leventer, A., Evangelinos, D., Escutia, C., and
1470 Mollenhauer, G.: Deglacial and Holocene sea-ice and climate dynamics in the Bransfield Strait, northern
1471 Antarctic Peninsula, *Clim. Past*, 19, 1061-1079, <https://doi.org/10.5194/cp-19-1061-2023>, 2023.
- 1472 Waelbroeck, C., Skinner, L. C., Labeyrie, L., Duplessy, J.-C., Michel, E., Vazquez Riveiros, N.,
1473 Gherardi, J.-M., and Dewilde, F.: The timing of deglacial circulation changes in the Atlantic,
1474 *Paleoceanography*, 26, <https://doi.org/10.1029/2010PA002007>, 2011.
- 1475 Weber, M. E., Bailey, I., Hemming, S. R., Martos, Y. M., Reilly, B. T., Ronge, T. A., Brachfeld, S.,
1476 Williams, T., Raymo, M., Belt, S. T., Smik, L., Vogel, H., Peck, V. L., Armbrecht, L., Cage, A., Cardillo,
1477 F. G., Du, Z., Fauth, G., Fogwill, C. J., Garcia, M., Garnsworthy, M., Glüder, A., Guitard, M., Gutjahr,
1478 M., Hernández-Almeida, I., Hoem, F. S., Hwang, J.-H., Iizuka, M., Kato, Y., Kenlee, B., Oconnell, S.,
1479 Pérez, L. F., Seki, O., Stevens, L., Tauxe, L., Tripathi, S., Warnock, J., and Zheng, X.: Antiphased dust
1480 deposition and productivity in the Antarctic Zone over 1.5 million years, *Nature Communications*, 13,
1481 2044, <https://doi.org/10.1038/s41467-022-29642-5>, 2022.
- 1482 Wei, W. and Lohmann, G.: Simulated Atlantic Multidecadal Oscillation during the Holocene, *Journal of*
1483 *Climate*, 25, 6989-7002, <https://doi.org/10.1175/JCLI-D-11-00667.1>, 2012.
- 1484 Williams, T. J., Martin, E. E., Sikes, E., Starr, A., Umling, N. E., and Glaubke, R.: Neodymium isotope
1485 evidence for coupled Southern Ocean circulation and Antarctic climate throughout the last 118,000
1486 years, *Quaternary Science Reviews*, 260, 106915, <https://doi.org/10.1016/j.quascirev.2021.106915>,
1487 2021.
- 1488 Xiao, W., Esper, O., and Gersonde, R.: Last Glacial - Holocene climate variability in the Atlantic sector
1489 of the Southern Ocean, *Quaternary Science Reviews*, 135, 115-137,
1490 <https://doi.org/10.1016/j.quascirev.2016.01.023>, 2016a.
- 1491 Xiao, W., Frederichs, T., Gersonde, R., Kuhn, G., Esper, O., and Zhang, X.: Constraining the dating of
1492 late Quaternary marine sediment records from the Scotia Sea (Southern Ocean), *Quaternary*
1493 *Geochronology*, 31, 97-118, <https://doi.org/10.1016/j.quageo.2015.11.003>, 2016b.
- 1494 Xiao, W., Xu, Y., Zhang, C., Lin, J., Wu, W., Lü, X., Tan, J., Zhang, X., Zheng, F., Song, X., Zhu, Y.,
1495 Yang, Y., Zhang, H., Wenzhöfer, F., Rowden, A. A., and Glud, R. N.: Disentangling Effects of Sea
1496 Surface Temperature and Water Depth on Hydroxylated Isoprenoid GDGTs: Insights From the Hadal
1497 Zone and Global Sediments, *Geophysical Research Letters*, 50, e2023GL103109,
1498 <https://doi.org/10.1029/2023GL103109>, 2023.
- 1499 Zhang, X., Knorr, G., Lohmann, G., and Barker, S.: Abrupt North Atlantic circulation changes in
1500 response to gradual CO₂ forcing in a glacial climate state, *Nature Geoscience*, 10, 518-523,
1501 <https://doi.org/10.1038/ngeo2974>, 2017.
- 1502 Zhang, X., Lohmann, G., Knorr, G., and Xu, X.: Different ocean states and transient characteristics in
1503 Last Glacial Maximum simulations and implications for deglaciation, *Clim. Past*, 9, 2319-2333,
1504 <https://doi.org/10.5194/cp-9-2319-2013>, 2013.
- 1505 Zhang, Y. G., Pagani, M., and Wang, Z.: Ring Index: A new strategy to evaluate the integrity of TEX₈₆
1506 paleothermometry, *Paleoceanography*, 31, 220-232, <https://doi.org/10.1002/2015PA002848>, 2016.
- 1507 Zielinski, U. and Gersonde, R.: Diatom distribution in Southern Ocean surface sediments (Atlantic
1508 sector): Implications for paleoenvironmental reconstructions, *Palaeogeography, Palaeoclimatology,*
1509 *Palaeoecology*, 129, 213-250, [https://doi.org/10.1016/S0031-0182\(96\)00130-7](https://doi.org/10.1016/S0031-0182(96)00130-7), 1997.
1510